Ocean Engineering 341 (2025) 122553

Contents lists available at ScienceDirect

Ocean Engineering

journal homepage: www.elsevier.com/locate/oceaneng

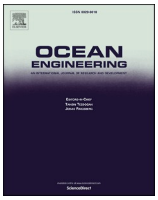

Research paper

Experimental validation of time domain simulations with HAMS-MREL and comparative analysis of linear and weakly nonlinear models for dense WEC arrays

Andreas T. Asiikkis [a,b], Vaibhav Raghavan [c], Dimokratis G.E. Grigoriadis [b], Andrei V. Metrikine [c], George Lavidas [c], Antonis I. Vakis [a,*]

[a] Computational Mechanical and Materials Engineering, Engineering and Technology Institute Groningen, University of Groningen, Nijenborgh 4, Groningen, 9747 AG, the Netherlands
[b] UCY-CompSci, Department of Mechanical & Manufacturing Engineering, University of Cyprus, 75 Kallipoleos, Nicosia, 1678, Cyprus
[c] Hydraulic Engineering Department, Delft University of Technology, Stevinweg 1, Delft, 2628 CN, Zuid Holland, the Netherlands

ARTICLE INFO

Keywords:
Wave energy converters
Dense WEC arrays
Hydrodynamic validation
HAMS-MREL
WEC-Sim
Nonlinear Froude-Krylov force

ABSTRACT

The accurate modelling of hydrodynamic interactions in dense arrays of Wave Energy Converters (WECs) is critical for optimizing design and predicting energy capture efficiency. This study presents the first time-domain experimental validation of the Boundary Element Method (BEM) multi body solver HAMS-MREL, for WEC arrays. The validation involves a comparative assessment of wave excitation forces from numerical predictions and physical measurements for an array of 5 floaters. Results exhibit good overall agreement, with Normalized Root Mean Square Error (NRMSE) values typically below 10 %, though with some exceptions. The results highlight solver limitations that vary with wave steepness and floater positioning within the array. Additionally, this study presents the first integration of HAMS-MREL with WEC-Sim for time-domain simulations, evaluating the linear HAMS-MREL and the weakly nonlinear WEC-Sim hydrodynamic models across various wave conditions. The comparative study conducted with the Ocean Grazer 4.0 case, a dense array of 18 floaters around a monopile, reveals the conditions under which linear modelling remains valid and when nonlinear approaches become necessary. Despite significant wave excitation force differences at wave steepness above 2 %, power output estimates remain within acceptable limits (~10 %). These findings offer critical insights into appropriate model selection for different wave conditions.

1. Introduction

Wave energy is a vast renewable resource that holds significant promise for diversifying the global energy mix and contributing to the decarbonization of the energy sector. Estimates put the global wave energy resource on the order of 2 TW (Gunn and Stock-Williams, 2012), indicating a substantial opportunity to meet future energy demand, while reducing greenhouse gas emissions. A wide variety of Wave Energy Converter (WEC) technologies have been developed to harness this resource (Zhang et al., 2021). These include conventional oscillating body devices, such as floating or fully submerged point absorbers (Sergiienko et al., 2017), as well as alternative concepts like Oscillating Water Columns (OWCs) (Rosati et al., 2022) and overtopping devices (Contestabile et al., 2020). These systems capture wave power through oscillating air in chambers, or overtopping reservoirs, respectively, rather than through the motion of buoyant bodies. In all cases, WECs employ a Power Take-Off (PTO) mechanism to convert the absorbed wave energy into electricity.

To maximize the energy captured from ocean waves, WEC arrays are a key concept (Vervaet et al., 2022), (Liu et al., 2025), (Wei et al., 2019). Unlike other renewables such as wind and tidal, hydrodynamic interactions between WECs can be constructive in nature and enhance the overall energy capture (Tay, 2022), (Chen et al., 2016). This approach increases the energy yield per unit area, making wave energy projects more feasible. However, designing effective WEC arrays requires careful consideration of complex hydrodynamic interactions between the devices and the surrounding stochastic wave environment (Yang et al., 2022).

---

* Corresponding author.
E-mail address: a.vakis@rug.nl (A.I. Vakis).

https://doi.org/10.1016/j.oceaneng.2025.122553
Received 27 June 2025; Received in revised form 9 August 2025; Accepted 20 August 2025

Accurate hydrodynamic modelling plays a critical role in the design and optimization of WEC systems before deployment (Sheng, 2019), enabling developers to evaluate and refine designs under a wide range of wave conditions. By predicting key hydrodynamic parameters—such as wave excitation forces, added mass, and radiation damping—numerical models along with optimization algorithms (Golbaz et al., 2022) provide insights that can guide the design process, ultimately leading to better performance, survivability, and cost efficiency. This predictive approach can significantly reduce costs and reliance on time-consuming experimental trials, thereby accelerating the development cycle of WEC technologies and subsequent array configurations.

Various numerical approaches are available to model WEC devices, each balancing fidelity and computational cost. The most popular choices include linear potential flow models based on the Boundary Element Method (BEM), weakly nonlinear models, and high-fidelity Computational Fluid Dynamics (CFD) models. BEM solvers compute the inviscid, linear wave-structure interaction problem efficiently in the frequency domain, and can be coupled to time-domain simulations, making them well suited for early-stage design studies and parametric array optimizations (Sheng, 2019). On the other hand, weakly nonlinear models like those based on Cummins equations (Cummins, 1962), extend BEM-based simulations by incorporating the instantaneous hydrostatic restoring and nonlinear Froude-Krylov (FK) forces. This is achieved by calculating the instantaneous wet surface at each time-step, with a relatively low computational-cost overhead (Katsidoniotaki et al., 2022). These models allow better representation of large body motions and steep waves without requiring a detailed CFD simulation.

CFD models, which solve the full Navier-Stokes equations, can capture complex nonlinear phenomena, including wave breaking, viscosity and turbulence, at the expense of substantially higher computational costs. Thus, CFD is generally reserved for scenarios where strong nonlinear wave-body interactions are important, such as extreme wave conditions or highly transient device responses that lie outside the assumptions of linear theory (Sheng, 2019). Comparative studies such as (Penalba et al., 2017a), (Giorgi et al., 2021), (Giorgi and Ringwood, 2018) have highlighted the value of weakly nonlinear models for single-body WECs in accurately capturing nonlinear Froude-Krylov forces and the time-varying wetted surface of buoys, especially under high wave steepness conditions or in the presence of PTO and control systems that significantly affect device motion. These weakly nonlinear models offer a balance between accuracy and computational cost, offering a practical alternative to fully nonlinear CFD approaches.

Several BEM codes are commonly used in WEC modelling, each of which has undergone varying degrees of validation. Notable examples include the open-source solvers Nemoh (Kurnia and Ducrozet, 2023) and Capytaine (Ancellin and Dias, 2019), the commercial codes WAMIT (WAMIT Inc.) and Ansys Aqwa (ANSYS Inc), and the recently developed solver HAMS-MREL suitable for multiple bodies (Raghavan et al., 2024a). All these codes can provide the hydrodynamic coefficients (added mass, radiation damping, wave excitation forces) as input to WEC-Sim (National Renewable Energy Laboratory and National Technology & Engineering Solutions of Sandia LLC (NTESS)), an open-source time-domain simulation tool which solves the equation of motion of WECs and provides the response of the bodies, constraints, moorings and PTOs involved in the system using the Cummin's equation. Nemoh was originally developed in Fortran and remains a widely used open-source code, while Capytaine is a more recent Python-based reimplementation of Nemoh. The commercial tools WAMIT and Ansys Aqwa have served as industry standards for wave structure interaction modelling and for validation of other BEM codes (Raghavan et al., 2024a), (Sun et al., 2023), (Penalba et al., 2017b).

HAMS-MREL (Hydrodynamic Analysis of Marine Structures – Marine Renewable Energies Lab), is a BEM solver developed by the Marine Renewable Energies Lab (MREL) at Delft University of Technology (TU Delft) (Raghavan et al., 2024a). This solver enhances the capabilities of the original HAMS code (Liu, 2019) by incorporating multiple body interaction formulations, allowing for the analysis of complex hydrodynamic interactions among multiple floating structures. HAMS-MREL V1.0 has been extensively validated against semi-analytical solutions and commercial solvers like WAMIT (Raghavan et al., 2024a), as well as through experimental data for an OWC device (Raghavan et al., 2024b), demonstrating its accuracy in both deep and finite water depths considering the hydrodynamic coefficients and exciting forces. The development of HAMS-MREL reflects a broader effort in the wave energy research community to advance BEM modelling tools for fast array analysis, providing researchers with more robust tools for the design and optimization of WECs and other offshore structures.

Despite considerable validation efforts of BEM codes for single-body WECs, experimental validations in time-domain involving multi-body configurations remain limited. Extensive single-body validation studies have been performed using various codes: Ruehl et al. (2014) first validated WEC-Sim for the case of an RM3 WEC, followed by more extensive validation tests in (Ruehl et al., 2016), (Tom et al., 2018), where WAMIT and Ansys Aqwa were used. Asiikkis et al. provided an experimental validation of Capytaine for single-body simulations under regular and irregular wave conditions (Asiikkis et al., 2023), (Asiikkis et al., 2025). Jin et al. (2023) validated a two-body attenuator-type WEC modelled in WEC-Sim with Ansys Aqwa BEM results. Ruiz et al. (2017) performed a muti-body validation study using experimental data for an array of five point-absorbers, with Nemoh V2 providing the hydrodynamic coefficients. These studies underscore the applicability of BEM solvers for individual and small groups of WECs, but few investigations have explored their performance in dense arrays, and none have experimentally validated the HAMS-MREL solver.

This study introduces, for the first time, the integration of the multi-body BEM solver HAMS-MREL into WEC-Sim, facilitating detailed time-domain simulations based on hydrodynamic coefficients computed by HAMS-MREL. While HAMS-MREL has been validated in the frequency domain (Raghavan et al., 2024a), no time-domain experimental validation has been conducted until now. In the first part of this work, we address this gap by comparing HAMS-MREL time-domain simulations with experimental data from the SWELL dataset (Faedo et al., 2023) for a five-device WEC array. Additionally, in the second part, this study compares the linear HAMS-MREL predictions with WEC-Sim's weakly nonlinear approach across a range of regular wave steepness conditions using a large-scale dense WEC array consisting of 19 bodies – the Ocean Grazer 4.0 (Asiikkis et al., 2024). Although previous studies have examined linear vs. weakly nonlinear models for single-body cases, this is the first to perform this comparison for a dense WEC array case. These contributions provide critical insights into the applicability of linear BEM modelling for large dense arrays under different wave conditions, and the benefit of using validated numerical tools for fast evaluation of WEC arrays.

2. Methodology

2.1. Overview of methodological framework

This study experimentally validates the BEM solver HAMS-MREL for modelling WEC arrays and assesses its applicability in large-scale, densely configured arrays through integration with WEC-Sim. The methodology is structured in two parts, each comprising two key steps, as illustrated in Fig. 1.

In the first part, the five-floater SWELL benchmark case (Faedo et al., 2023) is used to evaluate the numerical accuracy of HAMS-MREL. This includes (i) a mesh convergence study focused on wave excitation forces under regular wave conditions. Since the floaters are fixed in the experiments, the added mass and radiation damping were excluded from this convergence study. The second step (ii) is the experimental validation, where HAMS-MREL predictions are compared against measured wave excitation forces from the SWELL dataset.

The second part focuses on a large-scale, dense 19-body array (18

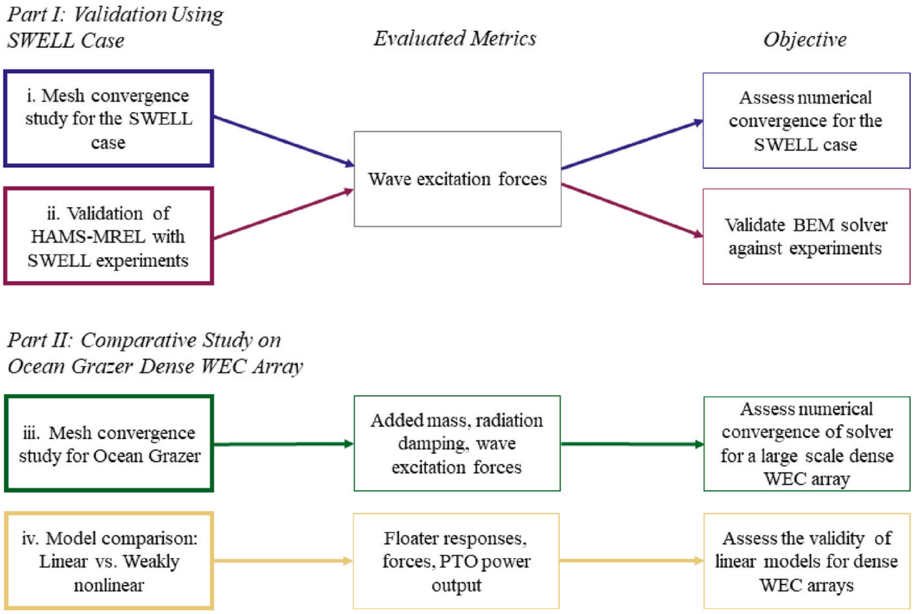

Fig. 1. Overview of the methodological framework used in this study. The process includes validation of HAMS-MREL and a comparative study of the linear and weakly nonlinear hydrodynamic models. Each step is evaluated based on key hydrodynamic metrics.

WECs and one monopile) based on the Ocean Grazer 4.0 concept (Asiikkis et al., 2024). This part includes (iii) a mesh convergence study for the Ocean Grazer array to ensure numerical stability of the computed hydrodynamic coefficients, and (iv) a comparative study where linear WEC-Sim simulations (using HAMS-MREL hydrodynamics as input) are compared against the weakly nonlinear WEC-Sim model (Lawson et al., 2014). The latter incorporates instantaneous nonlinear Froude–Krylov and hydrostatic forces. The two models are evaluated across a range of wave steepness conditions using key metrics, including floater responses, excitation forces, and power output, to assess the validity and limitations of linear modelling for dense WEC arrays.

This methodology provides a complete evaluation process for validating a BEM solver in both small- and large-scale array configurations and establishes a benchmark for comparing linear and weakly nonlinear hydrodynamic modelling approaches for a dense WEC array case.

2.2. Numerical modelling tools

2.2.1. Frequency-domain modelling with HAMS-MREL

The BEM is widely used for modelling wave-structure interactions at the early design stages of WECs. It provides a computationally efficient approach to solving the governing equations of potential flow theory in the frequency domain. This theory relies on the assumptions that the fluid is inviscid and that the flow is incompressible ($\nabla\cdot \boldsymbol{u} = 0$), and irrotational ($\nabla\times\boldsymbol{u}=0$), the waves are small relative to the wavelength and that the movements of the body are small relative to its geometric features (Mei, 1989). Under these conditions, the velocity field $\boldsymbol{u}$ can be represented as the gradient of a velocity potential ϕ as:

$$u=\nabla\phi, \tag{1}$$

where ϕ satisfies the Laplace equation in the entire fluid domain Ω, i.e.,

$$\nabla^2\phi=0, x\in\Omega. \tag{2}$$

This equation must be solved subject to boundary conditions on the free surface, the floating body surface, the seabed (if in finite depth) and at infinity. Depending on whether the body is fixed or free to move, the wave-structure interaction problem is categorized as either a diffraction problem, where an incident wave interacts with a fixed body, or a radiation problem, where a freely floating body oscillates and generates its own radiated waves.

Along the free surface at $z = 0$, the velocity potential must satisfy the linearized free surface condition:

$$\frac{\partial\phi}{\partial z}-\frac{\omega^2}{g}\phi=0, \tag{3}$$

where g is the gravitational acceleration and ω is the wave frequency.

For a finite depth h, a no-flow condition is set at the seabed:

$$\frac{\partial\phi}{\partial z}=0, z=-h. \tag{4}$$

On the body's surface ${S_B}^k$, the Neumann boundary condition ensures no fluid penetration. For the diffraction problem (fixed body), the normal velocity of the diffracted wave potential ϕ_D must be zero:

$$\frac{\partial\phi_D}{\partial n}=0, x\in {S_B}^k. \tag{5}$$

For the radiation problem (oscillating body), the normal velocity of the radiated wave potential ϕ_R is given by the body's motion:

$$\frac{\partial\phi_R}{\partial n}=n_j, x\in {S_B}^k, \tag{6}$$

where n_j is the normal component of the body motion in Degree of Freedom (DOF) j. These boundary conditions are incorporated in a Boundary Integral Equation (BIE), through which the velocity potential ϕ is computed. This approach directly incorporates boundary conditions into an integral equation defined over the surface of the body. For the diffraction problem, where an incident wave field interacts with a fixed body, the BIE is expressed as (Raghavan et al., 2024a):

$$2\pi\phi_S(x)+\iint_{S_B^T}\phi_S(\xi)\left(\frac{\partial G(\xi;x)}{\partial n_\xi}\right)dS_\xi=-\iint_{S_B^T}\left(\frac{\partial\phi_I}{\partial n}\right)G(\xi;x)dS_\xi, \tag{7}$$

where x and ξ are the field and source points respectively, G is the Green's function, and $S_B^T=S_B^1+S_B^2+\ldots+S_B^M$ is the total wetted surface of all M bodies. The terms ϕ_S and ϕ_I represent the scattered and incident wave potentials.

For the radiation problem, the BIE becomes:

$$2\pi\phi_j^k(x) + \iint_{S_B^T} \phi_j^k(\xi)\left(\frac{\partial G(\xi;x)}{\partial n_\xi}\right) dS_\xi = \iint_{S_B^k} G(\xi;x)\, n_j^k\, dS_\xi, \tag{8}$$

where ϕ_j^k is the radiation potential of the fluid because of body k ($k = 1, 2, \ldots, M$) and its DOF j. HAMS-MREL supports multi-body simulations and is well-suited for complex and dense WEC array configurations, as demonstrated in this study.

2.2.2. *Time-domain modelling with WEC-Sim*

WEC-Sim is an open-source numerical tool developed within the MATLAB/Simulink environment for simulating WEC dynamics. It was jointly created by the National Renewable Energy Laboratory (NREL) and Sandia National Laboratories to facilitate the efficient modelling of wave-induced motions and power extraction. The main advantage of WEC-Sim is its capability to evaluate the dynamic responses of floating bodies in the time domain with very low computational cost, allowing extensive parametric analyses and design optimizations.

WEC-Sim utilizes hydrodynamic parameters computed externally by frequency-domain BEM solvers, such as WAMIT, Nemoh, Ansys Aqwa and Capytaine. These parameters include the wave excitation forces, radiation damping, and added mass. Once obtained, WEC-Sim calculates the time domain response of the system by solving Newton's second law for rigid body dynamics, considering only the significant hydrodynamic and mechanical forces relevant to the analysis. The hydrodynamic model in WEC-Sim is based on the Cummins equation, which accounts for radiation memory effects through a convolution integral of the radiation impulse response function. For this study, the equation of motion of the floating bodies is expressed as:

$$m\,\ddot{\boldsymbol{X}}(t) = \boldsymbol{F}_{exc}(t) + \boldsymbol{F}_{rad}(t) + \boldsymbol{F}_B(t) + \boldsymbol{F}_{pto}(t), \tag{9}$$

where m is the mass of the floating body, $\ddot{\boldsymbol{X}}$ is the acceleration vector of the body and $\boldsymbol{F}_{exc}$ is the wave excitation force. $\boldsymbol{F}_{rad}$ is the radiation force, which in the full Cummins formulation includes the added mass at infinite frequency and a convolution integral of the radiation impulse response function. $\boldsymbol{F}_B$ is the buoyancy force and $\boldsymbol{F}_{pto}$ is the reaction force from the hydraulic Power Take-Off (PTO) system described later.

In this work, HAMS-MREL is integrated with WEC-Sim for the first time, enabling time-domain simulations of WECs and WEC arrays based on hydrodynamic coefficients computed by this solver. The integration is performed by feeding appropriately formatted input containing the hydrodynamic coefficient and excitation forces into BEMIO, which is part of WEC-Sim. In contrast, the weakly nonlinear WEC-Sim model, accounts for the nonlinear buoyancy and Froude-Krylov wave excitation forces by calculating these forces from the instantaneous water surface elevation and the actual position of each floater. Specifically, the static and dynamic pressures over the wetted body surface panels are calculated at each time step. This approach improves the accuracy of the buoyancy and Froude-Krylov force calculations, especially when significant variations in wetted surface area occur due to large body displacements under large wave steepness conditions. It is noted though that the weakly nonlinear model still utilizes the linear wave theory to determine the flow field and pressure distribution and is therefore not suitable for modelling highly nonlinear hydrodynamic events such as wave slamming or breaking. In particular, the radiation damping and added mass forces are still computed by the BEM solver (HAMS-MREL in this case). A more detailed description of the WEC-Sim formulation and the PTO dynamics can be found in (National Renewable Energy Laboratory and National Technology & Engineering Solutions of Sandia), (So et al., 2015).

2.2.3. *Limitations of the numerical models*

The modelling approaches used in this study have important assumptions and limitations that should be recognized before interpreting results. As with all potential flow-based BEM solvers, HAMS-MREL assumes inviscid, incompressible, and irrotational flow, and does not capture viscous effects such as drag, flow separation, or vortex shedding, which may become important in specific operating regimes, especially under high wave steepness or large amplitude motion. Furthermore, the linear wave theory employed in both the linear and weakly nonlinear WEC-Sim models neglects wave breaking and turbulence. While the weakly nonlinear model improves the prediction of FK and hydrostatic forces, by accounting for the instantaneous free-surface elevation, it still assumes linear wave kinematics and does not alter the hydrodynamic coefficients. These limitations should be acknowledged, especially under steep wave conditions or in cases where viscous effects become significant.

3. Part 1: experimental validation of time-domain simulations with HAMS-MREL

3.1. *SWELL dataset and physical setup*

The accuracy of the numerical models was assessed by comparing their predictions against experimental data from the open-access SWELL dataset (Standardized Wave Energy Converter Array Learning Library) (Faedo et al., 2023). This dataset consists of a series of wave basin experiments conducted at Aalborg University in Denmark, focusing on the hydrodynamics of WEC arrays. The dataset is a valuable benchmark for validating numerical models, as it includes a diverse range of WEC layouts and wave conditions.

The effective test area of the wave basin was 13 m × 8 m and the depth was set at 0.9 m, as shown in Fig. 2. Waves were generated with a 30-segment wavemaker and active absorption was utilized. The dataset includes a comprehensive array of sensors for capturing the wave elevation at various points in the wave tank, and the hydrodynamic loads acting on the WECs. These loads were measured using load cells mounted on the fixed WECs.

The experiments included multiple layouts of floating point absorbers, arranged in different formations. For this study, we focus on Layout 7 (as mentioned in the original publication), which consists of four floaters in a row configuration and a fifth floater behind them. The floaters used in the experiments were 1:20 scale models of the Wavestar WEC, a well-established point absorber concept.

SWELL includes various test types, but for this study, we focus on Test 1 and Test 2. The former provides surface elevation measurements without the presence of floaters, which is used as the input wave elevation in the simulations. The latter provides the measured wave excitation forces on fixed WECs. This allows for direct validation of the hydrodynamic predictions from HAMS-MREL, independent of PTO effects. The forces were recorded for five different regular wave conditions, covering a range of frequencies relevant to WEC's operational response, as detailed in Table 1. These waves were selected to cover low-, mid-, and high-frequency conditions.

The experimental setup ensured high-precision data acquisition, with a sampling frequency of 200 Hz for all measurements while the specific instruments with their uncertainties are listed in Table 2. Importantly, although the dataset variable *excitationForce_WE* refers to an excitation force, it is actually measured at point B along the arm which is connected to the floater and not at the center of the floater, as shown in Fig. 2. Therefore, this does not correspond to a direct measurement of the total heave or surge excitation force acting on the floater. Instead, the variable *excitationTorque_WE* which is the wave excitation torque about the hinge point A, is used for validation.

This torque is derived via post-processing the experimental measurements, by combining the measured force at point B with the known geometry, as detailed in (Faedo et al., 2023). Since this torque captures the overall wave-induced moment on the floater, it provides a physically consistent quantity for comparison with numerical models. To enable direct comparison with the experimental torques, the wave excitation forces obtained in the simulations were post-processed to compute the

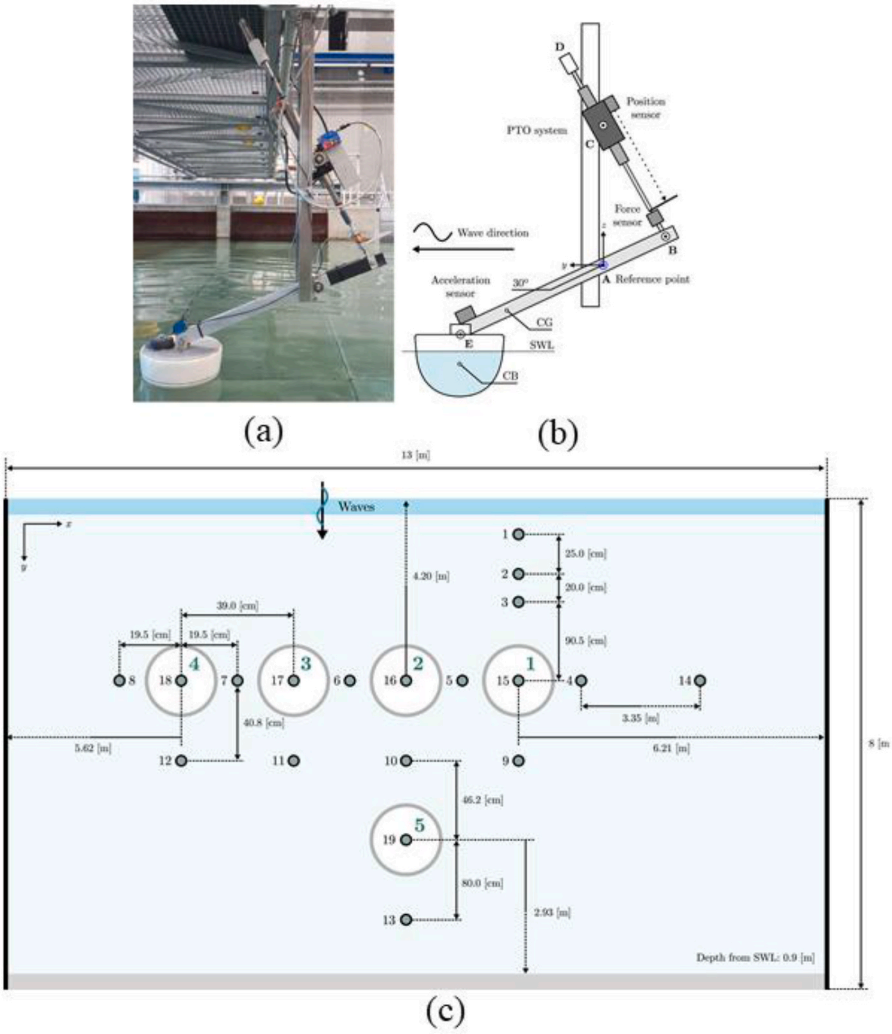

Fig. 2. Experimental setup of the SWELL benchmark case (Layout 7, taken from (Faedo et al., 2023)). (a) The test facility showing one of the five Wavestar floaters equipped with instrumentation. (b) Schematic of the floater setup illustrating the location of sensors and reference points. (c) Top view layout of the 5-floater array within the wave basin including spacing dimensions.

Table 1
Regular wave conditions used in Test 1 of the SWELL experiments. All tests were conducted with an approximately constant wave height of ∼0.05 m and varying wave periods from 0.8 to 1.5 s, with each run lasting 60 s (Faedo et al., 2023).

ID	Type	Mean Wave Height $\boldsymbol{H}$ [m]	Wavelength λ [m]	Wave Steepness $\frac{\boldsymbol{H}}{\boldsymbol{\lambda}}[-]$	Mean Wave Period $\boldsymbol{T}$ [s]	Length of experiments [s]
RSS1	Regular	0.052	1.00	0.052	0.80	60
RSS2	Regular	0.053	1.27	0.042	0.90	60
RSS3	Regular	0.043	1.57	0.028	1.0	60
RSS4	Regular	0.045	3.57	0.013	1.2	60
RSS5	Regular	0.052	4.46	0.012	1.5	60

corresponding torque about point A, as described in the next section.

3.2. Numerical setup for SWELL

To solve the BIE, HAMS-MREL requires the geometry of floating bodies to be discretized into surface panels. In this study, the Wavestar floaters were meshed at four levels of discretization—ranging from coarse to fine—with 48, 453, 727, and 1481 panels per floater, respectively. This mesh convergence study allows the assessment of how the numerical resolution of the floaters influences the accuracy of HAMS-MREL predictions.

The input parameters used for the HAMS-MREL simulations are summarized in Table 3. A wave heading of 0° was maintained throughout, and the frequency range extended up to 15 rad/s to ensure that high-frequency behavior was captured.

For time-domain simulations in WEC-Sim, the wave input was based on Test 1 of the SWELL experimental dataset. Each floater in the array was modelled as a fixed body, as shown in the Simulink model in Fig. 3. A fixed time step of 0.005 s using the WEC-Sim solver ode4 was used to match the frequency resolution of the experimental setup and satisfy the recommendation of WEC-Sim to resolve the wave period by 100–200 time-steps (National Renewable Energy Laboratory and National

Table 2

Description of measurements, sensors and uncertainties used in the SWELL experiments (Faedo et al., 2023).

Variable Name in the SWELL dataset	Description	Units	Measurement Source	Uncertainty
waveElevation_WE	Wave elevation at probes 1 to 14	m	Wave gauges (VTI WG-8CH)	±0.04 mm
excitationForce_WE	Wave excitation force (at point B)	N	Load cell (Futek LSB302)	±0.125 N
excitationTorque_WE	Wave excitation torque (computed at point A)	Nm	Computed from force at point B	Derived

Table 3

Input parameters used in the HAMS-MREL simulations for the SWELL case, including environmental conditions, wave characteristics, and mesh resolutions.

Parameters	Value	Units
Wave Heading	0	°
Wave Frequency	0.2 : 0.187 : 15	rad/s
Depth	0.9	m
Density	1000	kg/m^3
Number of panels to resolve the wet surface of the floater	48 453 727 1481	[−]

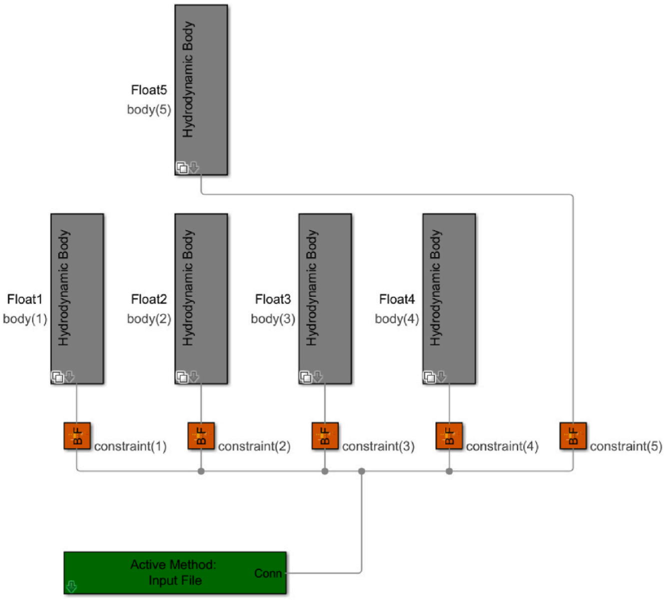

Fig. 3. Simulink model in WEC-Sim representing the five-floater array for the SWELL test case. Each floater is modelled with a fixed constraint.

Technology & Engineering Solutions of Sandia). To avoid initial transient effects at the beginning of the simulation, a ramp time of 10 s was applied, and simulations were run for a total of 60 s to align with the duration of the experiments.

The hydrodynamic output from WEC-Sim is the wave excitation force acting on each floater. However, the experimental data used for validation are expressed in terms of the wave excitation torque τ_A about the hinge point A. The computed torque from the simulations was obtained using the following expression:

$$\tau_A = F_{exc,z} L_{AE} \sin(\theta) + F_{exc,x} L_{AE} \cos(\theta) \quad (10),$$

where $\theta = 30^\circ$ is the angle between the arm and the horizontal, $F_{exc,z}$ and $F_{exc,x}$ are the vertical and horizontal components of the wave excitation force, and L_{AE} is the distance from the hinge point A to the force application point E on the floater (see Fig. 2).

3.3. Mesh convergence study for SWELL

First, a mesh convergence analysis was conducted for the SWELL validation case to ensure numerical convergence of the HAMS-MREL solver results, specifically targeting the accuracy of wave excitation torque predictions since these values are used for the validation later. Four mesh discretizations were tested, ranging from a coarse mesh with 48 panels to progressively finer meshes with 453, 727, and 1481 panels per floater. Fig. 4 illustrates the excitation torque for each floater over a 20-second period under these discretizations.

Performing this convergence analysis is crucial to balance accuracy with computational efficiency. As expected, the relative CPU time and memory usage significantly increase with finer discretization as can be seen in Table 4. Specifically, when comparing the coarse (48-panel) mesh to the finest (1481– panel) mesh, computational time increased by a factor of 185, with RAM usage rising from 1 GB to 8 GB. The intermediate meshes (453 and 727 panels) showed computational cost increases by factors of 15 and 37, respectively, with memory usage maintained relatively low (1–2 GB). A quantitative error analysis was also conducted by calculating the Normalized Root Mean Square Error (NRMSE) between successive meshes. The NRMSE is defined as the root mean square error between torque signals normalized by the range of the reference signal over the quasi-steady-state period ($t > 10$ s). The NRMSE between the 453 and 727 meshes was just 0.021%, and between 727 and 1481 it was 0.064%, indicating that convergence was already effectively achieved at 453 panels.

The torque predictions in Fig. 4 demonstrate clear convergence as the mesh refinement increases. Initial discrepancies between coarse and finer meshes gradually diminish, with results for the 453-, 727- and 1481-panel meshes aligning, indicating numerical convergence. Specifically, minor differences are observed in peak torques and signal phases, especially noticeable in the zoomed-in inserts provided for each floater. The slight reduction in peak torque observed for the 1481 panel mesh can be explained by the over-discretization effects, where a dense panel discretization can affect the pressure integration. Overall, the differences become negligible between the three finest discretizations, supporting the conclusion that the 727-panel mesh provides a suitable balance between computational cost and accuracy for the SWELL test case. This sensitivity analysis thus confirms that using a mesh of 727 panels is appropriate for subsequent validation studies and simulations, achieving reliable predictions of wave excitation torques while maintaining reasonable computational demands.

3.4. Results and discussion: validation against experimental data

The numerical predictions of wave excitation torque obtained using HAMS-MREL were validated against experimental measurements from the SWELL dataset for five distinct regular wave conditions (RSS1 – RSS5). This validation primarily aimed at evaluating the solver's predictive accuracy across a range of wave steepness conditions while also addressing a gap in the literature by validating a BEM code's capability to accurately predict excitation forces within dense WEC arrays.

Fig. 5 shows the phase-averaged excitation torque signals derived from both simulations and experiments for each floater and wave condition. The phase averaging was performed by isolating the complete wave cycles after the ramp time, aligning them based on their phase, and averaging the corresponding time samples within each cycle. This process yields a consistent signal that represents the steady-state excitation

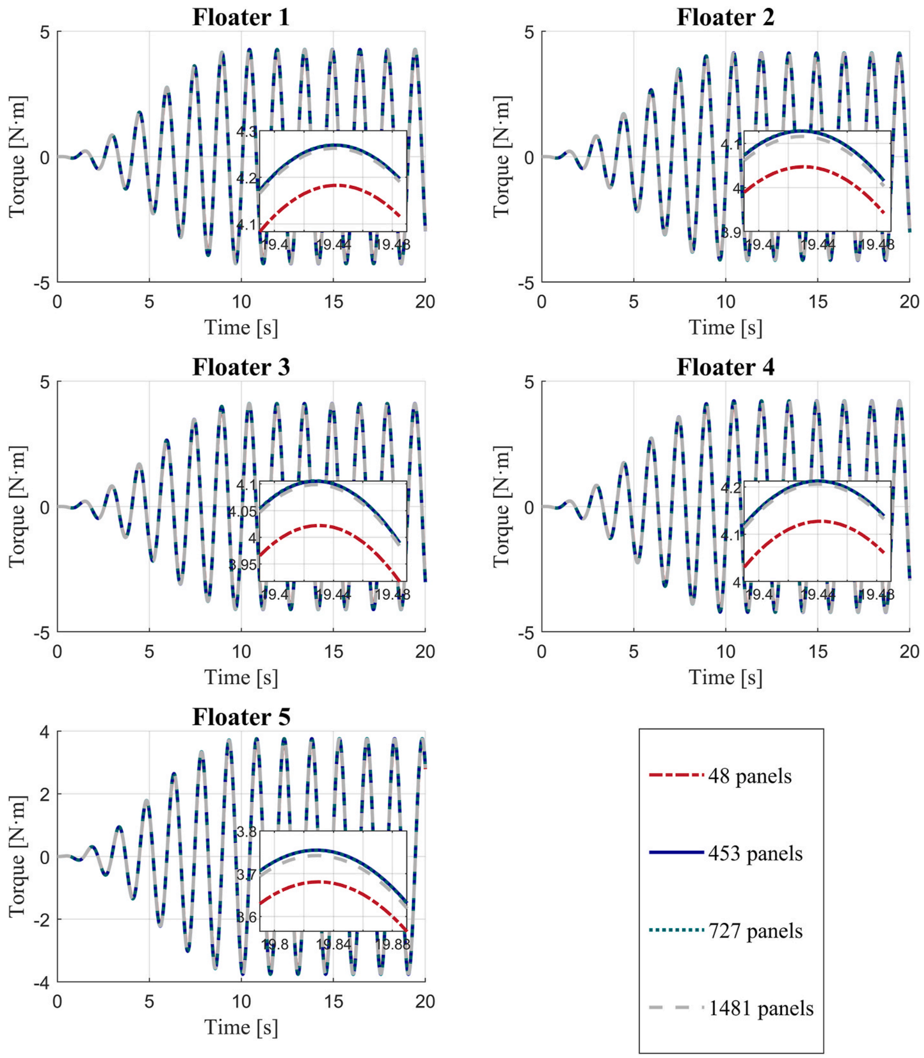

Fig. 4. Time history of wave excitation torque using HAMS-MREL, for each of the five floaters under four different mesh discretizations with 48, 453, 727, and 1481 panels. The zoomed-in insets highlight the differences in peak values and signal alignment.

Table 4

Computational cost and Normalized Root Mean Square Error (NRMSE) for each mesh discretization used in the SWELL case. CPU time is scaled relative to the lowest mesh case (48 panels). NRMSE is calculated for the excitation torque over the quasi-steady-state interval (10–20 s) between successive mesh refinements.

Mesh resolution (Panels)	Relative CPU Time	RAM Usage [GB]	NRMSE [%]
48	1	1	–
453	15	1	0.76
727	37	2	0.021
1481	185	8	0.064

response under regular wave forcing. Overall, there is a good agreement for most conditions and floaters, indicating that HAMS-MREL effectively captures the dynamics of wave-body interactions.

To quantify the accuracy of these predictions, the Normalized Root Mean Square Error (NRMSE) was calculated for each torque signal across all floaters and wave conditions, shown in Fig. 6. The NRMSE values ranged from approximately 2–21%, with notably higher discrepancies observed for the downstream floater (Floater 5). Specifically, Floater 5 exhibited particularly high NRMSE values (17–19%) under the higher wave steepness conditions (RSS1–RSS3), highlighting challenges in accurately modelling downstream hydrodynamic interactions at greater steepness levels. Conversely, the other floaters demonstrated consistently good agreement, typically yielding NRMSE values below 10%, with occasional exceptions such as Floater 3 under the RSS2 condition. It is also important to acknowledge that part of the observed discrepancies may be also attributed to experimental uncertainties. In particular, the wave input used in the simulations was taken from a separate test (Test 1) in which floaters were absent, whereas the measured excitation forces correspond to Test 2, where the floaters were present. Any variations in wave conditions between these two experimental runs, due to wave generator repeatability or effects from the active absorption, could introduce inconsistencies between the simulated and actual wave fields, thus affecting the accuracy of the validation results. Additionally, the linear potential flow model assumes not only an inviscid irrotational flow but also a constant wetted surface area throughout the simulations, which is of course not the case in the experiments, especially under higher wave steepness.

In Fig. 7 further analysis of torque signal characteristics, including maxima, minima, and amplitudes, provide deeper insights into the accuracy of the solver. Differences between predicted and measured maxima and minima ranged widely, from negligible deviations (around 1%) to substantial differences of up to 56%. These variations emphasize the sensitivity of local hydrodynamics to the positioning within the array, particularly impacting the downstream floater (Floater 5). For Floater 5, a notable trend emerges when comparing numerical accuracy against wave steepness: lower wave steepness conditions (RSS4 and

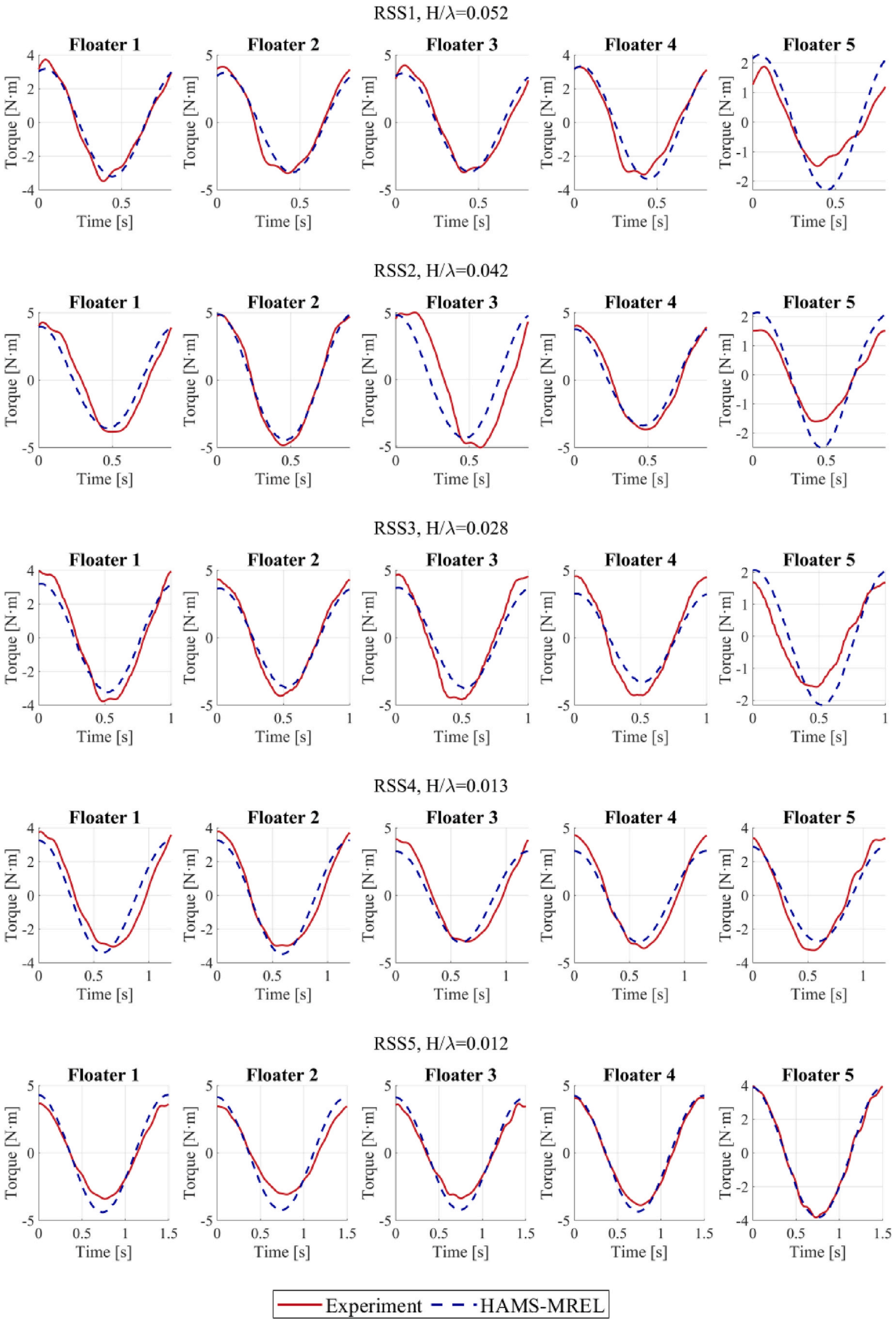

Fig. 5. Comparison of phase-averaged wave excitation torque signals between HAMS-MREL simulations (dashed blue) and experimental measurements (solid red) for all five floaters under five regular wave conditions (RSS1 – RSS5).

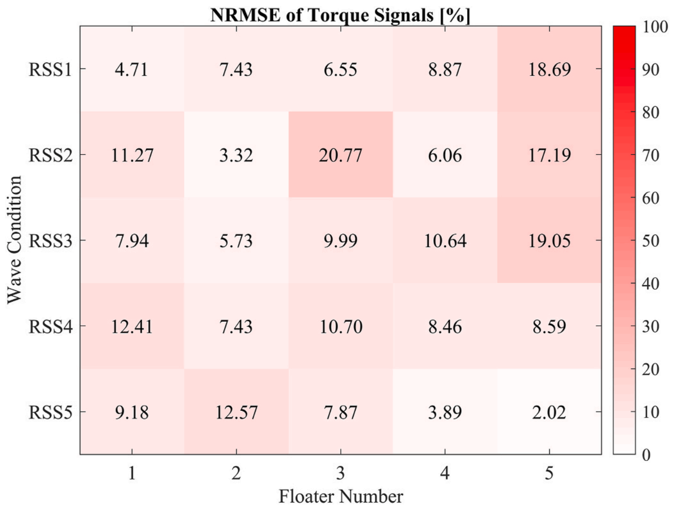

Fig. 6. Normalized Root Mean Square Error (NRMSE, %) of excitation torque signals across all the floaters and wave conditions.

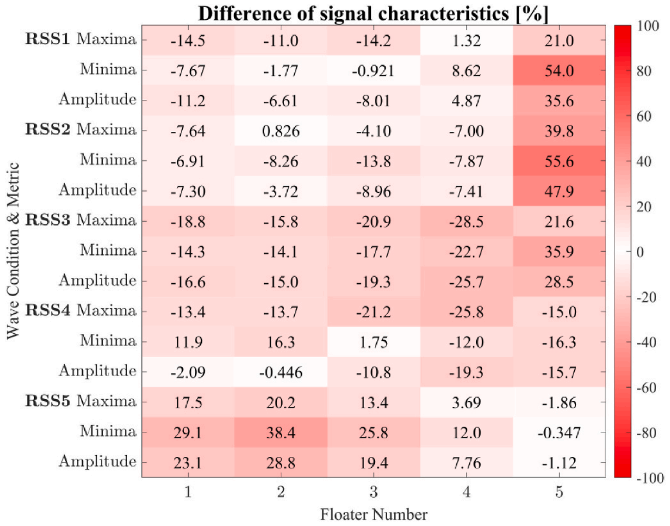

Fig. 7. Percentage difference in signal characteristics (maxima, minima, amplitude) of the excitation torque between HAMS-MREL simulations and experiments across all floaters and wave conditions.

RSS5) tend to produce better agreement between simulations and experiments. Interestingly, however, floaters 1 – 4 showed greater discrepancies at lower steepness values, especially under the RSS5 condition. Specifically, for the RSS5 condition, numerical predictions consistently overestimated the wave excitation torque. This behavior may result from multiple factors including the lower frequencies associated with RSS5, which correspond to higher wave induced pressures acting on the array. Conversely, for floaters 1– 4 in conditions RSS1–RSS4, the amplitude of wave excitation forces was generally underestimated. This discrepancy could partly arise from shorter wavelengths ($\sim$ 1–1.5 m) at higher frequencies, which are comparable to the floater spacing (ranging between 0.6–1.1 m), potentially inducing local diffraction, scattering and interference effects not fully captured by linear theory. Additionally, higher steepness conditions introduce nonlinear Froude-Krylov forces due to the large changes of floaters' wet surface, further contributing to the differences observed.

This validation study demonstrates that HAMS-MREL reliably predicts wave excitation torques across various wave steepness scenarios, achieving particularly good accuracy under moderate conditions. However, higher steepness scenarios should be interpreted cautiously, as the increased nonlinearities in such conditions can limit the predictive capability of linear potential flow-based methods.

4. Part 2: comparative study of the HAMS-MREL linear model vs. a weakly nonlinear model with nonlinear Froude-Krylov forces

4.1. Ocean Grazer 4.0 dense WEC array: configuration and simulation setup

The Ocean Grazer (OG) 4.0 represents a novel concept in wave energy conversion, featuring a dense array of 18 point absorber WECs arranged in a compact honeycomb configuration around a monopile wind turbine, as illustrated in Fig. 8. This layout enables high power extraction per unit sea surface area by focusing on strong hydrodynamic interactions between neighboring floaters. Each buoy is modelled as a vertical cylindrical body with a conical bottom, having a diameter of 5 m and a mass of 26, 111 Kg.

A fully integrated hydraulic Power Take-Off (PTO) system is modelled, based on a standardized hydraulic architecture optimized according to the guidelines established by Asiikkis et al. (2024), where a full parametric analysis and optimization was performed to select these values for maximizing power output. Each floater is coupled to an individual PTO unit as shown in Fig. 9, comprising a piston-cylinder assembly, rectifying check valves, gas-charged hydraulic accumulators, a hydraulic motor, and an electric generator. This architecture enables bidirectional energy harvesting during both the upstroke and downstroke of the buoy.

The heave motion of the buoy drives a double-acting piston that displaces fluid from two chambers (A and B). The pressure difference generated across these chambers produces the PTO force, defined as:

$$F_{PTO} = (p_A - p_B)A_p \quad (11),$$

where p_A and p_B are the pressures in chambers A and B, respectively, and A_p is the piston cross-sectional area. The hydraulic fluid passes through a rectifying check valve system, ensuring unidirectional flow into the accumulators. The high-pressure accumulator (HPA) and low-pressure accumulator (LPA) store and regulate the hydraulic energy before it is converted into mechanical energy by the hydraulic motor. This motor drives an electric generator to produce electricity. The complete PTO layout and component interconnection are illustrated in Fig. 10 which shows the Simulink implementation of a single PTO unit. The diagram includes Simulink blocks representing each physical subsystem: the hydraulic piston modelling the flows through the chambers and the reactive PTO force, the check valve logic, the connections of the accumulators, the hydraulic motor's flow-to-torque conversion, and the equivalent electric generator circuit controlled by a PI controller. These Simulink blocks model the physical energy conversion process from wave-induced motion of the floaters to electrical output. A summary of all the values used to specify the PTO of this test case are given in Table 5.

4.2. Mesh convergence study

Similarly to the SWELL test-case, a mesh convergence study is carried out to determine the appropriate surface discretization for simulating the Ocean Grazer WEC array using HAMS-MREL. The input parameters for the simulations of this section are shown in Table 6. Three mesh resolutions were tested: a coarse, medium and fine one consisting of 657, 1241 and 1825 panels, respectively. Their evaluation is based on their effect on the main hydrodynamic coefficients: added mass, radiation damping, and wave excitation force in the heave direction. The results are presented in Fig. 11 for three representative floaters (Body 1, 9, and 14), positioned at the front middle, and rear of the array, respectively, to capture a comprehensive view of the spatial variability of forces induced by multi-body interactions. It is noted that all hydrodynamic quantities

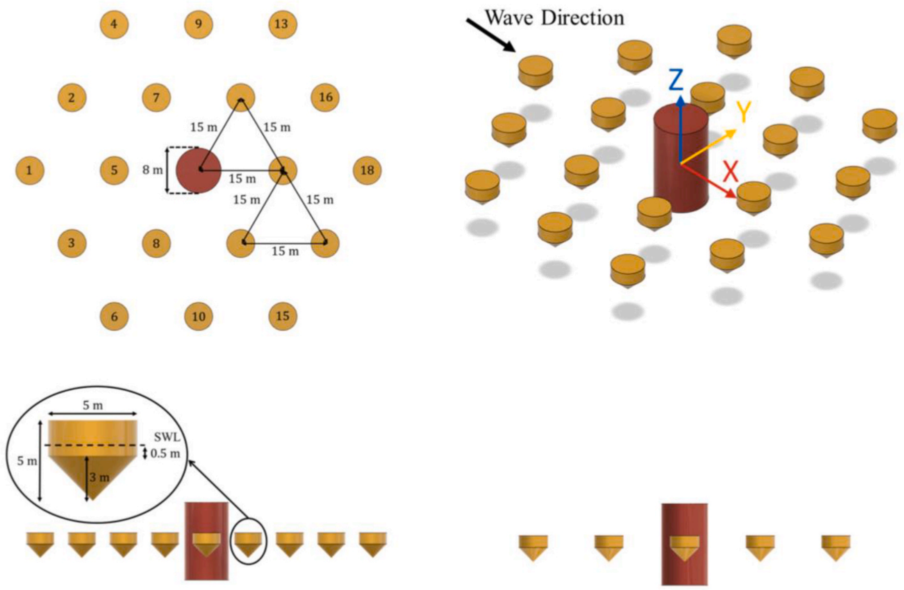

Fig. 8. The Ocean Grazer array of 18 WECs arranged in a dense honeycomb configuration around a central monopile, including the dimensions, wave direction and coordinate system (adopted from (Asiikkis et al., 2024)).

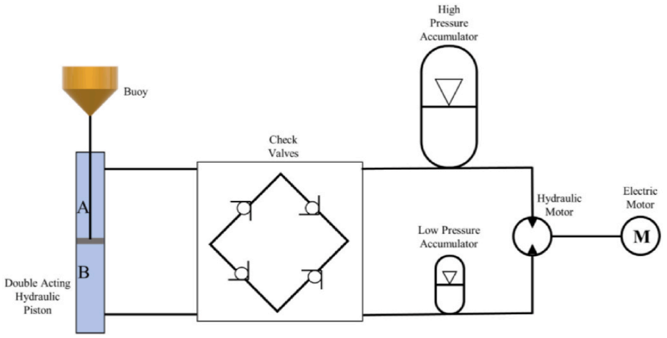

Fig. 9. Schematic of the hydraulic PTO architecture. Each buoy is coupled to a double-acting hydraulic piston that drives fluid through a rectifying check valve assembly into two accumulators. The stored hydraulic energy is subsequently converted to mechanical and then electrical power using a hydraulic motor and an electric generator (adopted from (Asiikkis et al., 2024)).

are normalized: the wave excitation force as $X_j/(\rho g)$, the added mass as $A_{i,j}/\rho$, and the radiation damping as $B_{i,j}/(\rho\omega)$.

Across all floaters and hydrodynamic coefficients, the medium and fine meshes yield identical results, confirming numerical convergence. The coarse mesh also captures the overall trends well but introduces small localized discrepancies at specific frequencies. For example, the excitation force of Floater 14 shows deviations near $\omega = 3.8$ rad/ s, and the added mass of Floater 9 differs slightly around $\omega = 3.2$ rad/ s, as shown in Fig. 11. These differences are attributed to the reduced surface resolution of the floater geometry, which affects the pressure integration on the body surface. This kind of mesh sensitivity is expected in dense arrays, where complex wave-body interactions amplify the influence of discretization. Since these discrepancies vanish with mesh refinement, the medium mesh is considered sufficiently accurate across the full frequency range analyzed (0.4–8 rad/s).

From a computational standpoint, the choice of mesh has a significant impact. To ensure consistency in performance benchmarking, all simulations were performed on the DelftBlue supercomputer at Delft University of Technology, equipped with a single Intel Xeon E5-6448Y, 32-core, 2.1 GHz processors. Table 7 details the relative computational cost and peak memory usage for the three mesh resolutions. Simulating with the finer mesh is almost 15 times more computationally demanding than the coarse mesh and over three times more demanding than the medium mesh. Moreover, the fine mesh required a maximum of 223 GB of RAM during execution, compared to 105 GB for the medium mesh. The medium mesh therefore offers a practical balance between numerical fidelity and computational efficiency.

Based on the convergence behavior and the resource requirements, the medium mesh is selected for the remainder of the Ocean Grazer simulations. This ensures accurate representation of multi-body hydrodynamics while maintaining feasible computational demands, particularly important given the scale of the array and the number of frequencies simulated.

4.3. *Results and discussion: linear vs. weakly nonlinear modelling*

This section presents a comparison between the linear hydrodynamic model implemented by HAMS-MREL and the weakly nonlinear model in WEC-Sim. The main distinctions between the two models lie in how the Froude-Krylov and buoyancy forces are treated, as summarized below:

- HAMS-MREL linear model: Computes the linear Froude-Krylov, buoyancy, added mass, and radiation damping forces based on linear potential flow theory and the mean wetted surface.
- WEC-Sim weakly nonlinear model: Computes the nonlinear Froude-Krylov and buoyancy forces based on the instantaneous wetted surface and floater position. The added mass and radiation damping are still taken from the linear HAMS-MREL BEM solution.

Initially, the temporal evolution of selected floaters is presented to illustrate how their position and forces acting upon them vary over time. The models are then compared across different wave conditions and floater locations to investigate spatial effects arising from nonlinear hydrodynamic interactions in a dense array configuration. Finally, the predicted power production from both models is compared for assessing the applicability and accuracy of the linear model across a range of wave scenarios. The wave conditions used in this study are summarized in Table 8. The wave period was set to 10 s to represent a typical long-period wave condition, while the wave height was varied to achieve steepness values H/λ ranging from 0.005 to 0.04. A fixed time step of 0.001 s using the WEC-Sim solver ode4 was used, with a total simulation

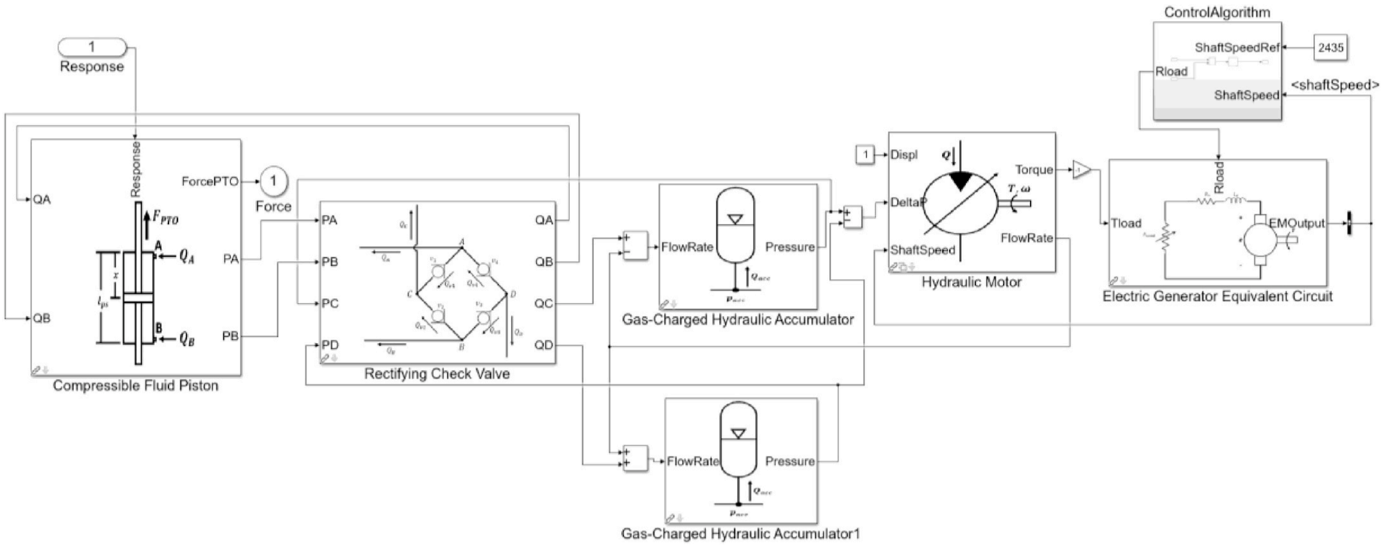

Fig. 10. Simulink model of the single hydraulic PTO system. The model includes all the components of the PTO: hydraulic piston, rectifying check valves, high and low pressure accumulators, hydraulic motor and an electric generator controlled by a PI controller.

Table 5
Geometrical, hydraulic, and electrical specifications of the WEC units and their respective PTO components used in the Ocean Grazer simulations, based on the design specifications reported by Asiikkis et al. (2024).

Parameter		Value	Units
Buoy Diameter		5	m
Buoy Mass		26111	kg
Moments of Inertia	I_{xx}	974400	kg m^2
	I_{yy}	974400	kg m^2
	I_{zz}	1204000	kg m^2
Diameter of piston		0.1038	m
Area of piston		0.008456	m^2
Stroke Limit		5	m
Piston Initial Pressure		20	MPa
HPA Pre-Charge Pressure		69	MPa
HPA Volume		0.051	m^3
LPA Pre-Charge Pressure		4	MPa
LPA Volume		0.01	m^3
Hydraulic Motor Displacement		66.7	cc/rev
Electric Generator Resistance (Ra)		0.0167	Ohm
Electric Generator (Ke)		1.85	V/(rad /s)
Electric Generator Inertia (Jem)		0.56	kg m^2
Electric Generator (bshaft)		0.01	(N m)/(rad /s)
Generator Speed		2435	rpm

Table 6
Input parameters used in the HAMS-MREL simulations for the Ocean Grazer case, including environmental conditions, wave characteristics, and mesh resolutions.

Parameters	Value	Units
Wave Heading	0	°
Wave Frequency	0.4 : 0.0962 : 8	rad/s
Depth	60	m
Density	1000	kg/m^3
Number of panels of the wet surface	657	[−]
	1241	
	1825	

time of 75 s for each case and a ramp time of 10 s. As shown in the results, this range spans a broad spectrum of wave conditions, from mild to highly steep waves, where the latter lead to significant nonlinear effects, including overtopping of the floaters.

4.3.1. *Temporal response of the array*

Fig. 12 illustrates the temporal evolution of heave displacement and total hydrodynamic forces acting on selected floaters (1, 5, 14, and 18) within the Ocean Grazer WEC array, comparing results from both the linear (HAMS-MREL) and weakly nonlinear (WEC-Sim) models under wave condition SS5 (see Table 8). The floaters selected, previously presented in Fig. 8, are located along the direction of wave propagation, upstream and downstream of the monopile, providing insights into nonlinear hydrodynamic interaction and wave shadowing phenomena.

Both modelling approaches show qualitatively similar heave displacement results, with peak-to-peak heave amplitudes of 1.72 m for upstream floaters (1 and 5) and slightly lower amplitudes of 1.70 m for downstream floaters (14 and 18). This subtle difference in amplitudes indicates the existence of small wave shadowing effects. However, the wave shadowing phenomenon is more pronounced when examining the total hydrodynamic forces acting on the floaters. Here, the total force refers to the sum of wave excitation, radiation damping, added mass and hydrostatic restoring components. The downstream floaters experience lower force amplitudes compared to the upstream floaters due to reduced wave energy availability behind the monopile.

Small but distinct differences between the linear and nonlinear model predictions become evident, especially near force maxima and minima, as highlighted by the red circles. These discrepancies occur because the weakly nonlinear model calculates excitation and restoring forces based on instantaneous free-surface elevations and wet areas of the floaters, capturing transient nonlinear wave-body interactions more accurately. In contrast, the linear model, relying on the frequency-domain linear assumption of a constant mean wet surface, tends to slightly overestimate these peak forces, as will be further explored in subsequent sections. This force overestimation is noticeable during phases of high floater acceleration near the zero-crossings, particularly at the negative peaks of the force, where the linear model produces larger excitation forces despite resulting in similar displacement response. In these cases, the nonlinear model captures the excitation force more accurately while still yielding comparable floater motions. This is attributed to the stiff dynamic response of the floater-PTO system, where small differences in hydrodynamic forces do not cause large variations in displacement.

These initial results establish an essential context regarding the temporal characteristics of the two modelling approaches, serving as a foundation for a detailed quantitative comparison across various wave conditions and spatial positions within the array presented in

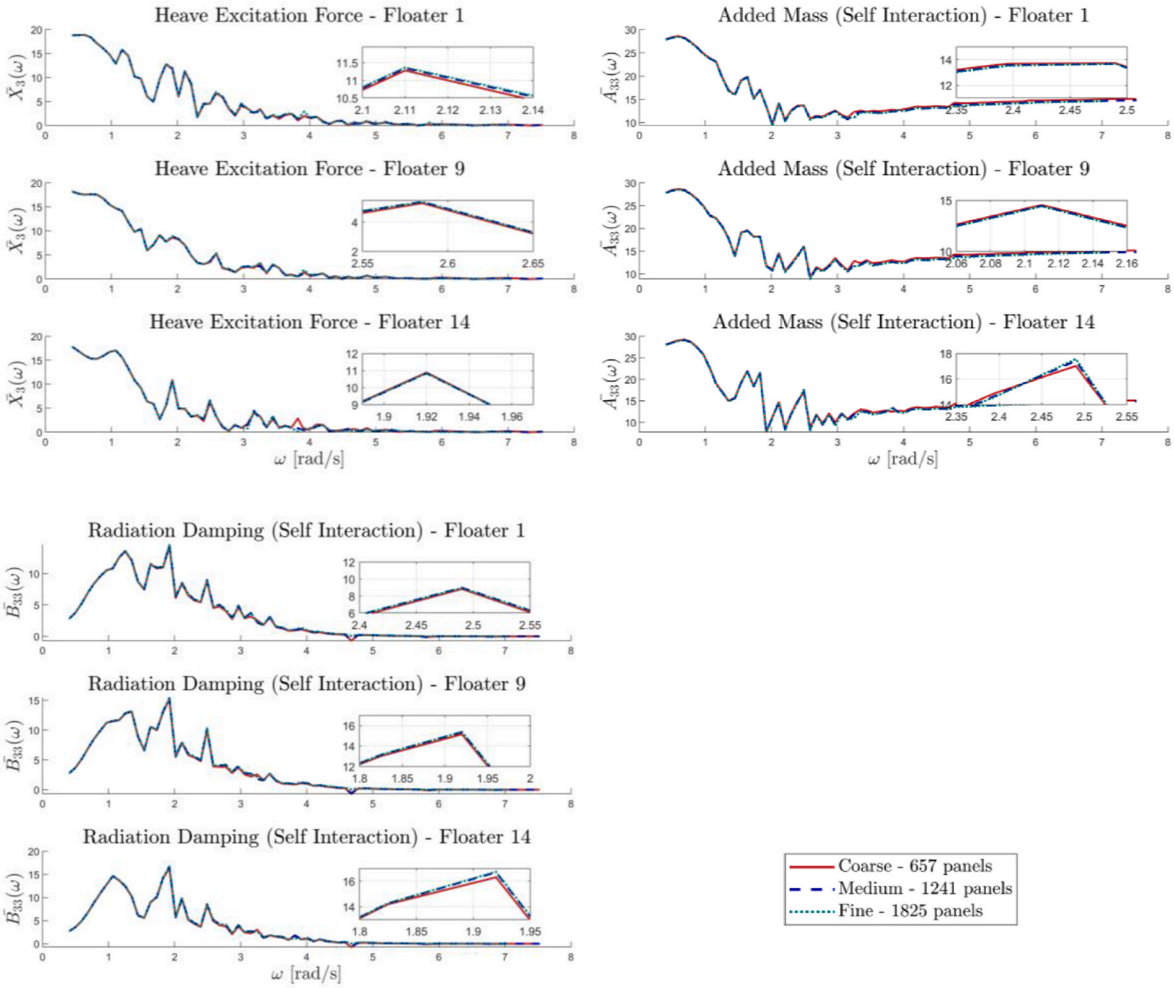

Fig. 11. Mesh convergence for the Ocean Grazer WEC array based on normalized heave-direction hydrodynamic coefficients (excitation force, added mass, radiation damping) computed for floaters 1, 9, 14, representing the front, middle, and rear array positions. Results for three mesh resolutions (coarse, medium, fine) are shown.

Table 7
Computational cost for each mesh discretization used in the Ocean Grazer case. CPU time is scaled relative to the coarser mesh case (657 panels per floater).

Mesh Panels	Relative CPU Time	RAM Usage [GB]
657	1	29
1241	4.6	105
1825	14.9	223

Table 8
Summary of regular wave conditions used in the comparative study between the linear and weakly nonlinear models. The wave period was fixed at 10 s, while wave height was varied to achieve a range of wave steepness values from 0.005 to 0.04.

Sea State (SS)	Wave Period T [s]	Wavelength λ [m]	Wave Steepness $\frac{H}{\lambda}$ [−]	Wave Height H [m]
SS1	10	148	0.005	0.74
SS2			0.010	1.48
SS3			0.015	2.22
SS4			0.020	2.96
SS5			0.025	3.70
SS6			0.030	4.44
SS7			0.035	5.18
SS8			0.040	5.92

subsequent sections.

4.3.2. *Excitation force trends across increasing wave steepness*

Fig. 13 provides deeper insights into the differences between the linear and weakly nonlinear hydrodynamic models through the phase-averaged excitation force acting on Floater 1, selected as it is the first body in the array encountering incoming waves, thus minimizing interference from other floaters and clearly revealing differences between the two models. Five wave conditions (SS1–SS5) with increasing wave heights and corresponding steepness are analyzed.

For the lowest wave steepness conditions SS1 and SS2 (with $H/\lambda = 0.005$ and 0.01, respectively), the linear and weakly nonlinear models predict nearly identical excitation forces, validating the applicability of linear theory under mild wave conditions where nonlinear effects are minimal. However, as wave steepness increases above $H/\lambda \gtrsim 0.015$ (SS3–SS5), notable discrepancies emerge between the two models, particularly near the maxima and minima of the excitation force, as shown in Fig. 13.

Specifically, for the steepest examined condition (SS5), the nonlinear model predicts a pronounced reduction in the positive peak of the phase-averaged excitation force. This time interval (3–5 s) corresponds to the upward movement of the floater. During this interval, the floater becomes fully submerged, causing a sharp reduction of 113 % in the excitation force followed by a rapid increase as the floater returns towards its mean position. Similarly, significant deviations are observed during the downward motion of the floater, where the nonlinear model's

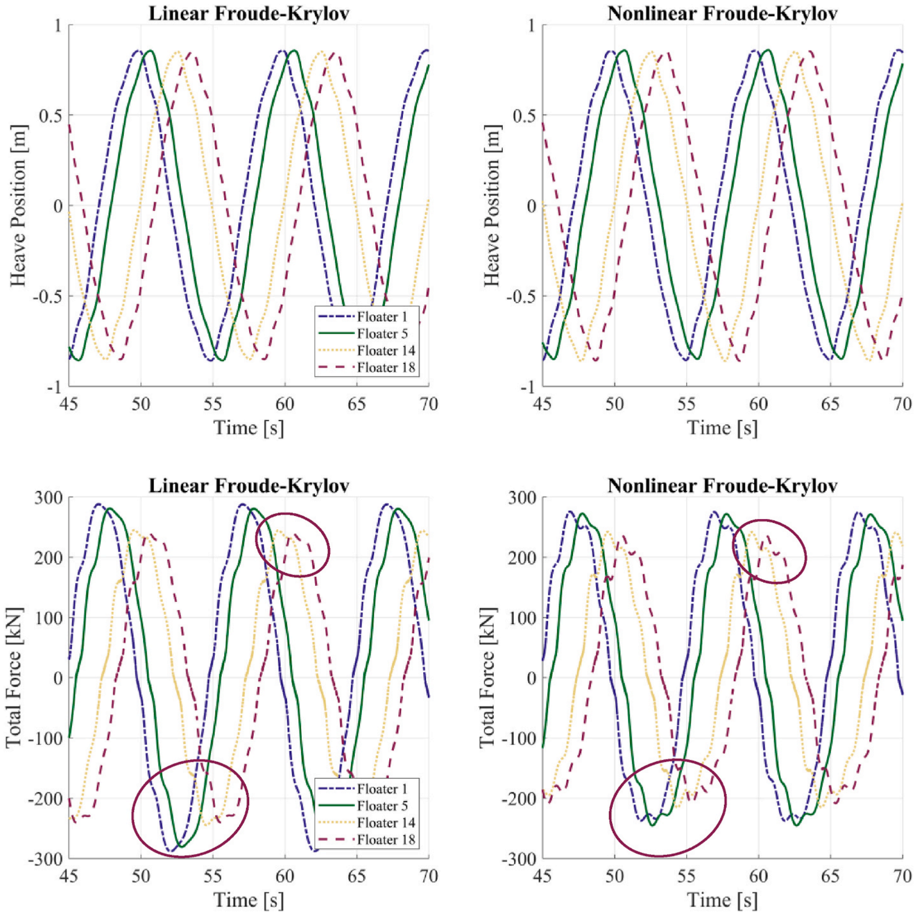

Fig. 12. Temporal evolution of heave displacement (top) and total hydrodynamic force (bottom) for floaters 1, 5, 14, and 18 in the Ocean Grazer WEC array under wave conditions SS5. Results from the linear HAMS-MREL model (left) and the weakly nonlinear WEC-Sim model (right) are shown. The red circles highlight differences between the two models at peak force values.

predictions are again substantially lower by 65 % than those from the linear model.

4.3.3. Analysis of hydrodynamic force components and instantaneous geometry effects

Fig. 14 illustrates all the hydrodynamic forces (left axis) acting on Floater 1 alongside its vertical positions (right axis) for both modelling approaches. The radiation damping and added mass coefficients used in both models are identical, since the weakly nonlinear model relies on the same BEM input data as the linear model. However, small differences appear in the added mass force shown in Fig. 14. This is expected, since the added mass force is computed in the time domain using the expression $F_{added\ mass}(t) = -A(\omega)\ddot{\boldsymbol{X}}(t)$. While the added mass coefficient $A(\omega)$ remains constant, the floater's acceleration $\ddot{\boldsymbol{X}}(t)$ varies slightly between the models due to differences in the excitation and restoring forces. Conversely, the wave excitation and hydrostatic restoring forces exhibit significant nonlinearities, especially evident as the floater passes through its mean position. Around 3–5 s in the wave cycle, as the floater moves upwards, the nonlinear excitation force decreases substantially, and at ~5 s, the restoring force suddenly becomes negative. This sharp reduction in the restoring force occurs due to the rapid decrease in submerged volume as the wave elevation begins to drop, contrasting significantly with the linear model's smoother predictions, which assume a constant submerged geometry.

To further clarify these observations, Fig. 15 presents the phase-averaged wetted surface area of Floater 1 across different wave steepness conditions (SS1-SS8). In the linear model, the wetter area is held constant at 36 m^2 based on the mean surface elevation, at all wave steepness conditions. For SS1, the nonlinear model shows identical results, confirming the negligible nonlinear effects at this low steepness. However, as steepness increases (SS2–SS4), moderate wetter area fluctuations emerge, corresponding to the slight differences observed earlier in the excitation forces (Fig. 13). For conditions SS5–SS8, the wetted area reaches its maximum possible value of 78.8 m^2, indicating full floater submergence. Conditions SS6–SS8 maintain full submergence for prolonged intervals (from 1.5 to 2.5 s). Such extended submergence periods may induce complex nonlinear flow phenomena not captured by WEC-Sim, including viscous effects. Thus, these conditions (SS6–SS8) were excluded from further analysis. This highlights the necessity of verifying floater submergence when using linear or weakly nonlinear models at high wave steepness to avoid unreliable results.

Returning to Fig. 14, it is clear why the linear model produces regular excitation and restoring forces, while the nonlinear model yields irregular and rapidly varying forces. Periods of full and minimal submergence correspond to the intervals of substantial deviation between the two models. This is also illustrated by Fig. 16, which shows snapshots of floater 1's vertical position through one wave cycle for SS5. At mid-cycle (around 4–5 s), the floater is fully submerged beneath the wave crest, directly correlating with the rapid decrease in excitation and restoring forces. Conversely, at the wave trough, minimal submergence similarly leads to significant deviations due to instantaneous geometry changes. Interestingly, despite considerable differences in hydrodynamic forces, both models predict nearly identical floater displacements.

These detailed analyses emphasize that linear modelling remains accurate at lower to moderate wave steepness but fails to capture critical nonlinear hydrodynamic behaviors at higher steepness. Consequently,

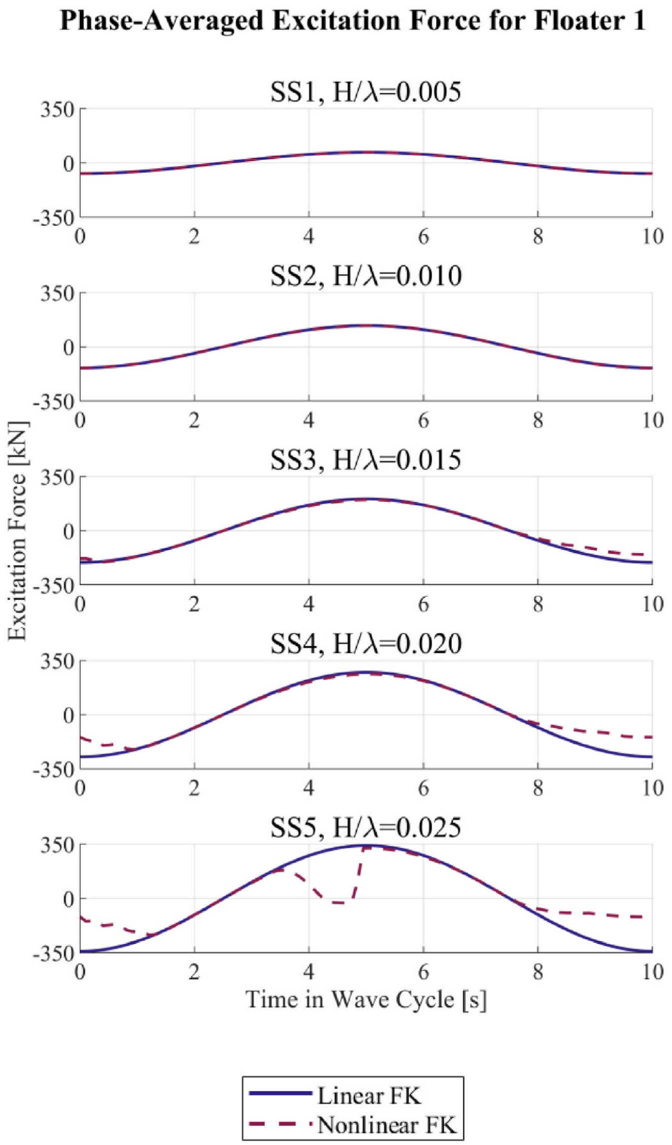

Fig. 13. Phase-averaged wave excitation force acting on floater 1 in the Ocean Grazer WEC array under five wave conditions (SS1-SS5) with increasing wave steepness. Results from the linear HAMS-MREL model and weakly nonlinear WEC-Sim model are compared.

incorporating nonlinear modelling becomes essential to reliably predict hydrodynamic structural loads under more steep wave conditions.

4.3.4. *Quantitative comparison of excitation forces and displacements*

To quantitatively compare the linear and weakly nonlinear models and thoroughly assess their accuracy, the NRMSE of the phase-averaged excitation forces was computed across five wave conditions (SS1-SS5), as presented in Fig. 17. The analysis encompasses selected floaters positioned differently within the array (front, side, and rear relative to the monopile) to investigate spatial differences.

At the lowest wave steepness conditions (SS1 and SS2), the NRMSE values remain below 1%, confirming that the linear model’s constant wetted-area assumption is valid under mild wave scenarios. With increasing wave steepness, however, the deviations progressively amplify. At SS3, the NRMSE slightly rises to approximately 3.5 – 4.5%, indicating modest yet acceptable differences between the two modelling approaches. Further increasing the wave steepness to SS4 results in a more pronounced divergence, with NRMSE values ranging between 10–12.5%. This suggests caution when applying linear assumptions at these intermediate steepness levels. For the highest examined steepness condition (SS5), the NRMSE substantially increases to a range of 18–25% clearly indicating that linear assumptions significantly deviate under such steep wave conditions. These observations show an exponential relationship between wave steepness and NRMSE of excitations forces, reinforcing the importance of carefully assessing the validity range for linear modelling based on specific device geometries and wave conditions.

To further clarify the practical implications of these differences, Fig. 18 presents the percentage differences in excitation force amplitudes between the two models across the same wave steepness conditions. Consistent with the NRMSE analysis, negligible amplitude differences of less than 1% are observed for low steepness conditions (SS1–SS3), supporting the suitability of linear modelling for mild conditions. Notably, even at SS3, despite the slight increase in NRMSE, amplitude differences remain minimal, confirming that linear predictions accurately capture peak excitation forces under these conditions. However, amplitude differences rise significantly at higher wave steepness values, reaching 11.5–15.5% for SS4 and 22.5–31% for SS5. This demonstrates not only a deviation in overall waveform shape but also a pronounced overestimation of force peaks by the linear model at higher steepness. Consequently, reliance on linear hydrodynamic assumptions, under these wave conditions, could lead to substantial overdesign in engineering applications.

In addition to excitation forces, Fig. 19 shows the NRMSE values of floater displacements between the two models. Interestingly, despite the notable differences observed in excitation forces, the displacement NRMSE values remain very low, below 2.5 % even for the highest steepness conditions (SS4 and SS5). At lower wave steepness (SS1–SS3), displacement differences are minor (below 1 %), supporting that linear assumptions provide highly accurate predictions of floater motions under these conditions. These results highlight that while linear modelling can provide reliable predictions for floater motions even under steep waves, significant inaccuracies in excitation forces at higher wave steepness could still influence structural and design considerations.

4.3.5. *Spatial distribution of model discrepancies across the array*

To explore spatial variations within dense WEC arrays, Fig. 20 provides the NRMSE distribution across all floaters for the wave steepness conditions SS3–SS5. At SS3, floaters located in front of the monopile exhibit slightly higher NRMSE values compared to those at the rear. This pattern can be explained by wave shadowing effects; front-row floaters directly encounter incoming waves, experiencing greater instantaneous wetted-area fluctuations compared to those in shadowed positions. In contrast, at SS4, this trend reverses, with rear floaters demonstrating higher NRMSE values. This behavior indicates that nonlinear wave interactions behind the monopile become significant enough at intermediate steepness conditions to amplify discrepancies relative to linear predictions. For the highest steepness case (SS5), the spatial distribution of NRMSE values is more complex, with increased values observed both at the front and rear positions, while floaters located in the second and third rows (centrally and on the sides) exhibit somewhat lower deviations. This mixed spatial response highlights the interplay of diffraction, shadowing, and nonlinear wave-body interactions at high wave steepness, emphasizing that model accuracy can vary substantially across the array depending on the wave conditions.

Furthermore, the monopile consistently shows minimal NRMSE values across all three conditions, which slightly increase with wave steepness but remain negligible. This is attributed to the monopile’s large surface area, resulting in minimal variations of the wet area even at high wave amplitudes, thus validating the continued suitability of linear assumptions for such fixed and large structures.

Overall, this analysis underscores the importance of selecting appropriate hydrodynamic modelling approaches, emphasizing the necessity of nonlinear modelling under moderate to high wave heights to

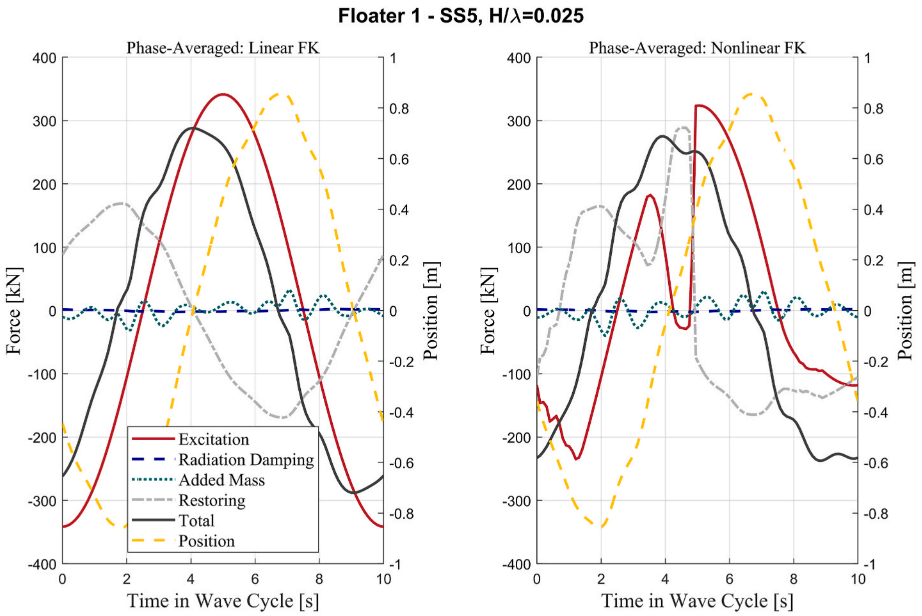

Fig. 14. Phase-averaged hydrodynamic forces acting on floater 1 of the Ocean Grazer WEC array for both the linear HAMS-MREL model (left plot) and the weakly nonlinear WEC-Sim model (right plot).

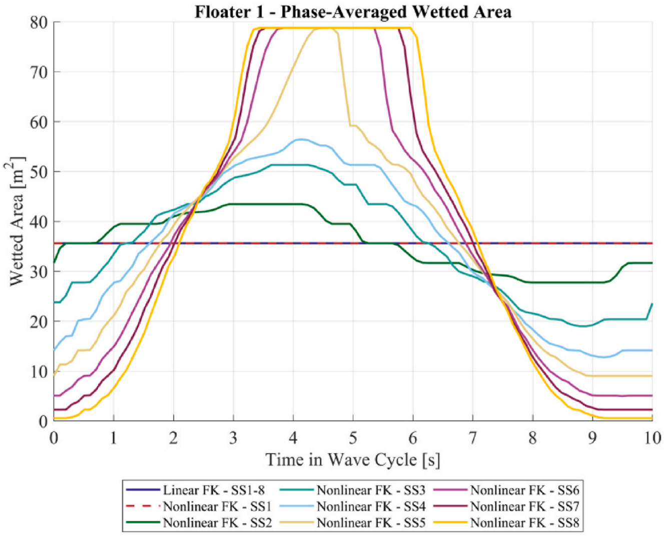

Fig. 15. Phase-averaged wetted surface area of floater 1 across wave conditions SS1-SS8, shown for both the linear HAMS-MREL model (solid blue line) and weakly nonlinear WEC-Sim model (all other lines).

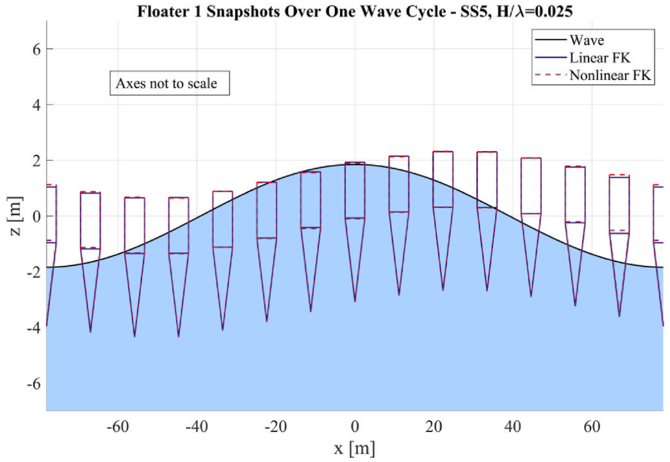

Fig. 16. Snapshots of floater 1's vertical position throughout one wave cycle under SS5, comparing the linear HAMS-MREL and weakly nonlinear WEC-Sim model and showing moments of full and minimal submergence. Axes are not to scale.

accurately predict structural loads and optimize WEC array designs.

4.3.6. Power output comparison between the linear and weakly nonlinear models

It is important to evaluate the practical implications of employing linear versus weakly nonlinear hydrodynamic models when predicting the power production capability of dense WEC arrays. Fig. 21 presents a comparison of the mean electrical power generated by the Ocean Grazer WEC array across wave steepness conditions SS1–SS5. The left plot compares the mean power output predicted by both modelling approaches, while the right plot quantifies the percentage differences for the entire array as well as for selected floaters.

Interestingly, at the lowest wave steepness (SS1), despite the hydrodynamic forces being nearly identical as discussed previously, the linear model underestimates the generated power by approximately 6 %. At intermediate wave steepness conditions (SS2–SS4), the deviation reduces, with the linear model slightly overestimating power by approximately 2.5–4.5%. However, at the highest wave steepness (SS5), the linear model significantly overestimates power production by approximately 10.5 %, underscoring the pronounced impact of nonlinear effects at higher wave steepness values. It is noteworthy that, although differences increase with wave steepness, overall power discrepancies are less pronounced compared to the substantial deviations observed in hydrodynamic forces, particularly the peak forces.

To further examine these discrepancies, the right plot in Fig. 21 provides detailed insights into percentage differences for selected individual floaters as well as for the entire array. For most wave conditions, excluding SS2, the individual floaters show similar trends in over- or underestimations. This consistent deviation across floaters indicates that nonlinear hydrodynamic predictions uniformly impact power output predictions for the entire array rather than affecting only specific areas.

These results carry significant implications for design and

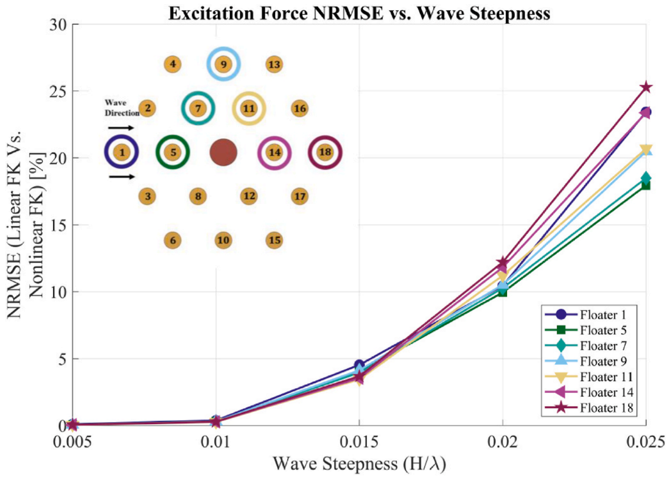

Fig. 17. Normalized Root Mean Square Error (NRMSE, %) of phase-averaged excitation forces between the linear HAMS-MREL and weakly nonlinear WEC-Sim models for selected floaters across increasing wave steepness (SS1-SS5). The inset shows the location of the analyzed floaters.

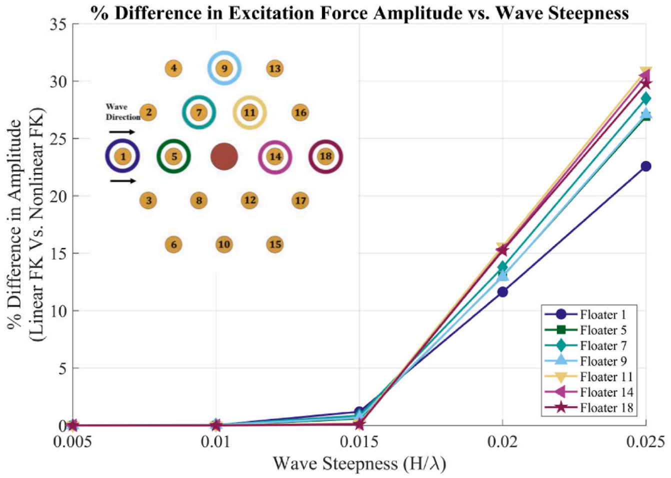

Fig. 18. Percentage difference in excitation force amplitude between the linear HAMS-MREL and weakly nonlinear WEC-Sim models for selected floaters across increasing wave steepness (SS1-SS5). The inset shows the location of the analyzed floaters.

operational decision-making. Relying on linear modelling under high wave steepness conditions could result in overly optimistic power production estimates, potentially leading to suboptimal economic and structural choices. Thus, while linear models may yield accurate power predictions at low to moderate wave steepness despite larger deviations in hydrodynamic forces, adopting nonlinear hydrodynamic models becomes essential for accurately predicting power output under higher wave steepness conditions.

5. Conclusions

This study was structured in two distinct parts. The first part focused on the experimental validation of the HAMS-MREL BEM solver using the SWELL dataset, which features a five-floater WEC array subjected to regular waves with wave steepness values ranging from 1.2 – 5.2%. HAMS-MREL was integrated with the WEC-Sim time-domain solver to simulate the wave excitation torques, which were then compared to experimental measurements. The results demonstrated good predictive accuracy across most conditions, with NRMSE values of wave excitation torques typically below 10 %. Notably, the downstream floater exhibited higher discrepancies under steep waves, with NRMSE values reaching 17–19%, at steepness values of 2.8–5.2%, indicating the limitations of applying the potential flow theory to model multi-body interactions under high wave steepness.

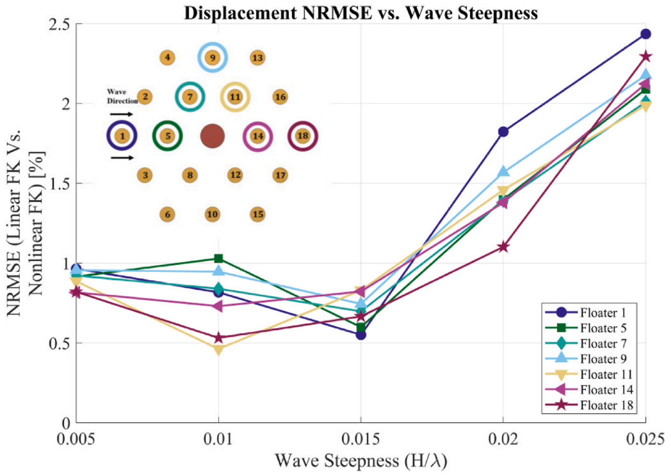

Fig. 19. Normalized Root Mean Square Error (NRMSE, %) of phase-averaged floater displacement between the linear HAMS-MREL and weakly nonlinear WEC-Sim models for selected floaters across increasing wave steepness (SS1-SS5). The inset shows the location of the analyzed floaters.

The second part of the study was focused on the comparative analysis between the linear HAMS-MREL and weakly nonlinear hydrodynamic model of WEC-Sim, for a large-scale WEC array: the Ocean Grazer 4.0 composed of 18 floaters arranged around a monopile. The linear model, based on the fixed wetted surface assumption, was shown to perform well under mild to moderate wave steepness (0.005–0.015), where NRMSE values of the excitation force remained below 5 %. However, for steeper waves (0.02–0.04), the linear model increasingly diverged from the weakly nonlinear approach due to its inability to account for the nonlinear Froude-Krylov forces which are calculated based on the instantaneous wetted surface and transient floater submergence. In these conditions, excitation force NRMSE values reached up to 25 %, overestimating force amplitudes by as high as 31 %. Despite these hydrodynamic discrepancies, the power output estimates showed only moderate differences, ranging from −6% to 10%. This indicates that while linear models may suffice for early-stage energy production analyses, they may lead to inaccuracies in structural performance predictions under highly nonlinear wave scenarios.

Overall, this study established a validated and computationally efficient modelling workflow using HAMS-MREL and WEC-Sim for dense WEC array simulations. It provides critical thresholds for the applicability of linear versus weakly nonlinear models in regular wave conditions.

Future work should expand the present validation study to include irregular and directional waves, and examine the influence of floater spacing and array layout on the fidelity of linear models relative to their weakly nonlinear counterparts. Furthermore, investigating the performance of the two models under extreme wave conditions by including viscous corrections, along with CFD comparative analysis, could provide additional insights into the limitations of potential flow theory and help define practical limits for its use in WEC simulations.

CRediT authorship contribution statement

Andreas T. Asiikkis: Writing – original draft, Visualization, Validation, Software, Methodology, Investigation, Formal analysis, Data curation, Conceptualization. **Vaibhav Raghavan:** Writing – review & editing, Software, Methodology, Investigation, Data curation, Conceptualization. **Dimokratis G.E. Grigoriadis:** Writing – review & editing,

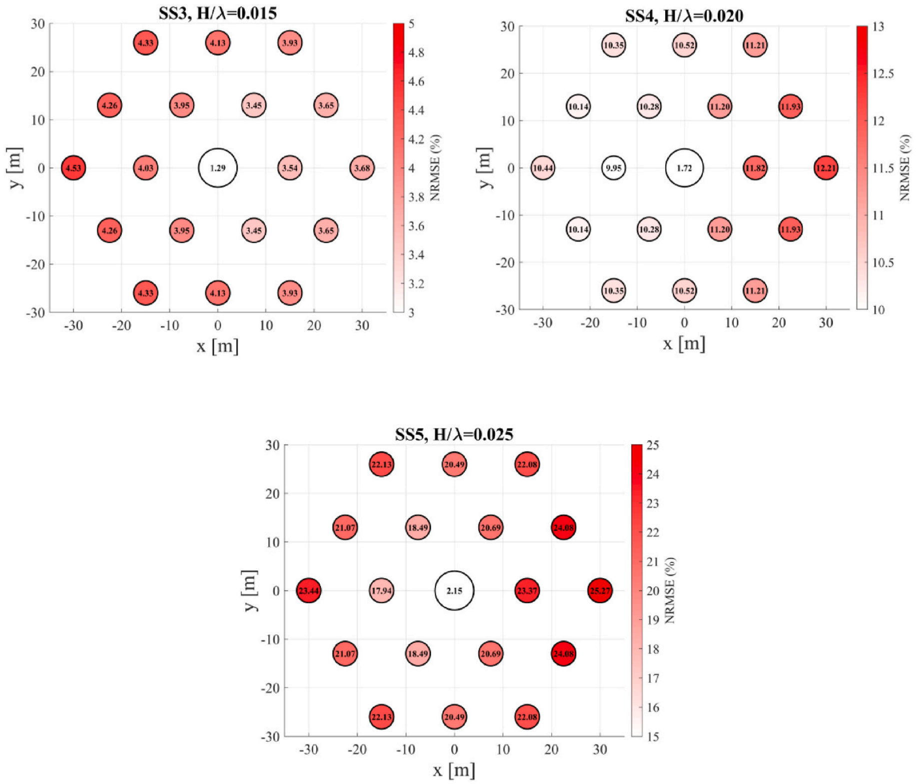

Fig. 20. Spatial distribution of Normalized Root Mean Square Error (NRMSE, %) of phase-averaged excitation forces between the linear HAMS-MREL and weakly nonlinear WEC-Sim models, across the Ocean Grazer WEC array, for three wave conditions (SS3-SS5).

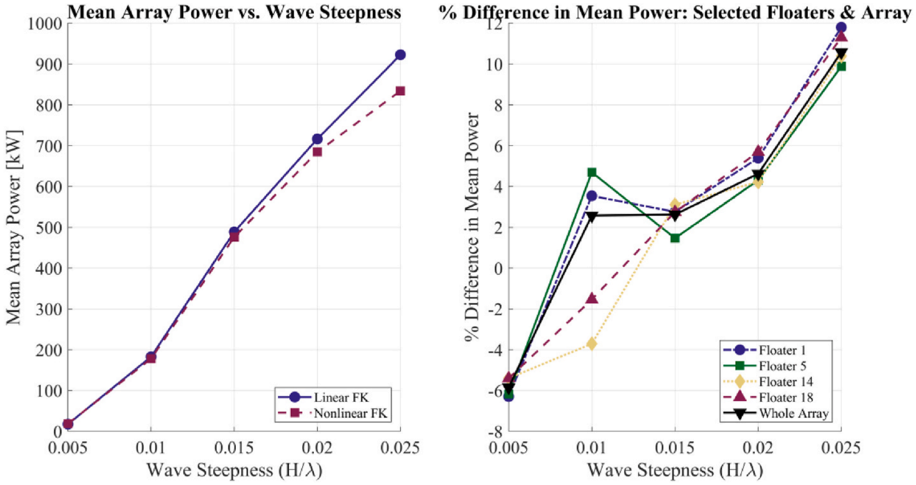

Fig. 21. Comparison of electrical power output between the linear HAMS-MREL model and the weakly nonlinear WEC-Sim model across increasing wave steepness (SS1–SS5). The left plot shows the mean power generated by the entire array, while the right plot presents the percentage difference between the two models for selected floaters and the full array.

Supervision, Project administration, Methodology, Funding acquisition, Conceptualization. **Andrei V. Metrikine:** Writing – review & editing, Supervision. **George Lavidas:** Writing – review & editing, Supervision, Methodology, Conceptualization. **Antonis I. Vakis:** Writing – review & editing, Supervision, Project administration, Methodology, Funding acquisition, Conceptualization.

Funding

This work was supported by Multimarine Services Ltd and CMMI – Cyprus Marine and Maritime Institute. CMMI was established by the CMMI/MaRITeC-X project as a “Center of Excellence in Marine and Maritime Research, Innovation and Technology Development” and has received funding from the European Union’s Horizon 2020 research and innovation program under grant agreement No. 857586; and by a matching funding from the Government of the Republic of Cyprus.

Declaration of competing interest

The authors declare that they have no known competing financial interests or personal relationships that could have appeared to influence the work reported in this paper.

References

Ancellin, M., Dias, F., 2019. Capytaine: a Python-based linear potential flow solver. J. Open Source Softw. 4 (36), 1341. https://doi.org/10.21105/joss.01341.

ANSYS Inc. Ansys aqwa. https://www.ansys.com/. (Accessed 27 January 2025).

Asiikkis, A., Grigoriadis, D., Vakis, A., 2023. Maximizing the surge amplitude of a floater through an adaptable mooring tightening technique. In: Proceedings of the European Wave and Tidal Energy Conference, vol. 15. https://doi.org/10.36688/ewtec-2023-274.

Asiikkis, A.T., Grigoriadis, D.G.E., Vakis, A.I., 2024. Wave-to-wire modelling and hydraulic PTO optimization of a dense point absorber WEC array. Renew. Energy 237 (Dec). https://doi.org/10.1016/j.renene.2024.121620.

Asiikkis, A.T., Grigoriadis, D.G.E., Vakis, A.I., 2025. Validation of capytaine for single-body hydrodynamic modelling using the SWELL experimental dataset. In: Proceedings of the 16th European Wave and Tidal Energy Conference. https://doi.org/10.36688/ewtec-2025-725. Funchal, Portugal.

Chen, W., Gao, F., Meng, X., Fu, J., 2016. Design of the wave energy converter array to achieve constructive effects. Ocean. Eng. 124, 13–20. https://doi.org/10.1016/j.oceaneng.2016.07.044.

Contestabile, P., Crispino, G., Di Lauro, E., Ferrante, V., Gisonni, C., Vicinanza, D., 2020. Overtopping breakwater for wave energy conversion: Review of state of art, recent advancements and what lies ahead. Renew. Energy 147, 705–718. https://doi.org/10.1016/j.renene.2019.08.115.

Cummins, W.E., 1962. The Impulse Response Function and Ship Motions.

Faedo, N., Peña-Sanchez, Y., Pasta, E., Papini, G., Mosquera, F.D., Ferri, F., 2023. SWELL: an open-access experimental dataset for arrays of wave energy conversion systems. Renew. Energy 212, 699–716. https://doi.org/10.1016/j.renene.2023.05.069.

Giorgi, G., Ringwood, J.V., 2018. Analytical representation of nonlinear Froude-Krylov forces for 3-DoF point absorbing wave energy devices. Ocean. Eng. 164, 749–759. https://doi.org/10.1016/j.oceaneng.2018.07.020.

Giorgi, G., Penalba, M., Gomes, R.P.F., 2021. Code-to-Code nonlinear hydrodynamic modelling verification for wave energy converters: WEC-Sim vs. NLFK4ALL. In: Proceedings of the 14th European Wave and Tidal Energy Conference. Plymouth, UK.

Golbaz, D., et al., 2022. Layout and Design Optimization of Ocean Wave Energy Converters: a Scoping Review of state-of-the-art Canonical, Hybrid, Cooperative, and Combinatorial Optimization Methods. Elsevier Ltd. https://doi.org/10.1016/j.egyr.2022.10.403

Gunn, K., Stock-Williams, C., 2012. Quantifying the global wave power resource. Renew. Energy 44, 296–304. https://doi.org/10.1016/j.renene.2012.01.101.

Jin, S., Wang, D., Hann, M., Collins, K., Conley, D., Greaves, D., 2023. A designed two-body hinged raft wave energy converter: from experimental study to annual power prediction for the EMEC site using WEC-Sim. Ocean. Eng. 267 (Jan). https://doi.org/10.1016/j.oceaneng.2022.113286.

Katsidoniotaki, E., Yu, Y.H., Göteman, M., 2022. Midfidelity model verification for a point-absorbing wave energy converter with linear power take-off. Int. Mar. Energy J. 5 (1), 67–75. https://doi.org/10.36688/imej.5.67-75.

Kurnia, R., Ducrozet, G., 2023. NEMOH: open-source boundary element solver for computation of first- and second-order hydrodynamic loads in the frequency domain. Comput. Phys. Commun. 292 (Nov). https://doi.org/10.1016/j.cpc.2023.108885.

Lawson, M., Yu, Y.-H., Nelessen, A., Ruehl, K., Michelen, C., 2014. Implementing nonlinear buoyancy and excitation forces in the WEC-Sim wave energy converter modeling tool. In: Volume 9B: Ocean Renewable Energy. American Society of Mechanical Engineers. https://doi.org/10.1115/OMAE2014-24445.

Liu, Y., 2019. HAMS: a frequency-domain preprocessor for wave-structure interactions-Theory, development, and application. J. Mar. Sci. Eng. 7 (3). https://doi.org/10.3390/jmse7030081.

Liu, T., Liu, Y., Huang, S., Xue, G., 2025. Influence of the hydraulic power take-off system on the dynamic response and power output of a wind-wave hybrid system. Appl. Ocean Res. 154 (Jan). https://doi.org/10.1016/j.apor.2024.104359.

Mei, C., 1989. In: The Applied Dynamics of Ocean Surface Waves, vol. 1. World Scientific Publishing.

National Renewable Energy Laboratory and National Technology & Engineering Solutions of Sandia, 'WEC-Sim', WEC-Sim (Wave Energy Converter Simulator). Accessed: May 7, 2025. [Online]. Available: wec-sim.github.io/WEC-Sim.

National Renewable Energy Laboratory and National Technology & Engineering Solutions of Sandia LLC (NTESS). WEC-Sim (Wave energy converter SIMulator). https://wec-sim.github.io/WEC-Sim/main/index.html. (Accessed 27 January 2025).

Penalba, M., Mérigaud, A., Gilloteaux, J.C., Ringwood, J.V., 2017a. Influence of nonlinear Froude–Krylov forces on the performance of two wave energy points absorbers. J. Ocean Eng. Mar. Energy 3 (3), 209–220. https://doi.org/10.1007/s40722-017-0082-x.

Penalba, M., Kelly, T., Ringwood, J., V Ringwood, J., 2017b. Using NEMOH for modelling wave energy converters: a comparative Study with WAMIT. In: 12th European Wave and Tidal Energy Conference. https://www.researchgate.net/publication/319160625.

Raghavan, V., Loukogeorgaki, E., Mantadakis, N., Metrikine, A.V., Lavidas, G., 2024a. HAMS-MREL, a new open source multiple body solver for marine renewable energies: model description, application and validation. Renew. Energy 237. https://doi.org/10.1016/j.renene.2024.121577.

Raghavan, V., Simonetti, I., Metrikine, A.V., Lavidas, G., Cappietti, L., 2024b. A new numerical modelling framework for fixed oscillating water column wave energy conversion device combining BEM and CFD methods: validation with experiments. Ocean. Eng. 301 (Jun). https://doi.org/10.1016/j.oceaneng.2024.117543.

Rosati, M., Henriques, J.C.C., Ringwood, J.V., 2022. Oscillating-Water-Column Wave Energy Converters: a Critical Review of Numerical Modelling and Control. Elsevier Ltd. https://doi.org/10.1016/j.ecmx.2022.100322

Ruehl, K., Michelen, C., Kanner, S., Lawson, M., Yu, Y.-H., 2014. Preliminary verification and validation of WEC-Sim, an open-source wave energy converter design tool. In: Volume 9B: Ocean Renewable Energy. American Society of Mechanical Engineers. https://doi.org/10.1115/OMAE2014-24312.

Ruehl, K., Michelen, C., Yu, Y.-H., Lawson, M., 2016. Update on WEC-Sim validation testing and code development. In: Proceedings of the 4th Marine Energy Technology Symposium, METS.

Ruiz, P.M., Ferri, F., Kofoed, J.P., 2017. Experimental validation of awave energy converter array hydrodynamics tool. Sustainability (Switzerland) 9 (1). https://doi.org/10.3390/su9010115.

Sergiienko, N.Y., Cazzolato, B.S., Ding, B., Hardy, P., Arjomandi, M., 2017. Performance comparison of the floating and fully submerged quasi-point absorber wave energy converters. Renew. Energy 108, 425–437. https://doi.org/10.1016/j.renene.2017.03.002.

Sheng, W., 2019. Wave energy conversion and hydrodynamics modelling technologies: a review. Renew. Sustain. Energy Rev. 109, 482–498. https://doi.org/10.1016/j.rser.2019.04.030.

So, R., Simmons, A., Brekken, T., Ruehl, K., Michelen, C., 2015. Development of PTO-Sim: a power performance module for the open-source wave energy converter code WEC-Sim. In: Volume 9: Ocean Renewable Energy. American Society of Mechanical Engineers. https://doi.org/10.1115/OMAE2015-42074.

Sun, S.L., Tian, J., Zhou, X.Q., Li, H., 2023. Investigation of a Weathervaning FPSO Based on a Fully Nonlinear Boundary Element Method. Springer Science and Business Media B.V. https://doi.org/10.1007/s11071-023-08694-2.

Tay, Z.Y., 2022. Effect of resonance and wave reflection in semi-enclosed moonpool on performance enhancement of point absorber arrays. Ocean. Eng. 243 (Jan). https://doi.org/10.1016/j.oceaneng.2021.110182.

Tom, N., Ruehl, K., Ferri, F., 2018. Numerical model development and validation for the WECCCOMP control competition. In: Volume 10: Ocean Renewable Energy. American Society of Mechanical Engineers. https://doi.org/10.1115/OMAE2018-78094.

Vervaet, T., Stratigaki, V., De Backer, B., Stockman, K., Vantorre, M., Troch, P., 2022. Experimental modelling of point-absorber wave energy converter arrays: a comprehensive review, identification of research gaps and design of the WECfarm setup. J. Mar. Sci. Eng. 10 (8). https://doi.org/10.3390/jmse10081062.

WAMIT Inc.. Wamit. https://www.wamit.com/index.htm. (Accessed 12 March 2025).

Wei, Y., Bechlenberg, A., van Rooij, M., Jayawardhana, B., Vakis, A.I., 2019. Modelling of a wave energy converter array with a nonlinear power take-off system in the frequency domain. Appl. Ocean Res. 90 (Sep). https://doi.org/10.1016/j.apor.2019.05.009.

Yang, B., et al., 2022. Wave Energy Converter Array Layout Optimization: a Critical and Comprehensive Overview. Elsevier Ltd. https://doi.org/10.1016/j.rser.2022.112668

Zhang, Y., Zhao, Y., Sun, W., Li, J., 2021. Ocean Wave Energy Converters: Technical Principle, Device Realization, and Performance Evaluation. Elsevier Ltd. https://doi.org/10.1016/j.rser.2021.110764.